Computers & Fluids 70 (2012) 29–43

Contents lists available at SciVerse ScienceDirect

Computers & Fluids

journal homepage: www.elsevier.com/locate/compfluid

Open boundary conditions for the velocity-correction scheme of the Navier–Stokes equations

A. Poux [a,*], S. Glockner [a], E. Ahusborde [b], M. Azaïez [a]

[a] Université de Bordeaux, IPB-I2M UMR CNRS 5295, 33607 Pessac, France
[b] Laboratoire de Mathématiques et de leurs Applications (U.M.R. 5142 CNRS), Batiment IPRA, Université de Pau et des Pays de l'Adour, France

ARTICLE INFO

Article history:
Received 8 December 2011
Received in revised form 2 July 2012
Accepted 29 August 2012
Available online 21 September 2012

Keywords:
Navier–Stokes equations
Projection methods
Velocity-correction methods
Fractional step methods
Open boundary condition
Pressure boundary condition
Bifurcated tube
Square cylinder
Backward-facing step

ABSTRACT

In this paper we propose to study open boundary conditions for incompressible Navier–Stokes equations, in the framework of velocity-correction methods. The standard way to enforce this type of boundary condition is described, followed by an adaptation of the one we proposed in [36] that provides higher pressure and velocity convergence rates in space and time for pressure-correction schemes. These two methods are illustrated with a numerical test with both finite volume and spectral Legendre methods. We conclude with three physical simulations: first with the flow over a backward-facing step, secondly, we study, in a geometry where a bifurcation takes place, the influence of Reynolds number on the laminar flow structure, and lastly, we verify the solution obtained for the unsteady flow around a square cylinder.

1. Introduction

Efficiently reaching an accurate solution to the unsteady incompressible Navier–Stokes equations is difficult for two main reasons. Firstly, the treatment of non-linearities and secondly, the determination of the pressure field which will ensure a solenoidal velocity field. From all the methods that address this second matter we can sort them in two categories: exact and approximative methods. In the first one, there are all the methods based on the idea proposed by Uzawa et al. [3], like those in [10,16]. In complex geometries or three-dimensional domains, this turns out to be inappropriate since its computational time costs become very high. Augmented Lagrangian is an iterative method described by Fortin and Glowinski in [14]. With this method computing the exact solution is possible but also very costly. Nevertheless an accurate approximation of the solution can be obtained with a small number of iterations. This leads to faster computations but without exactly respecting the incompressibility constraint. The method of interest in this article is one of an another class of non-exact methods which consists in decoupling the pressure from the velocity by means of a time-splitting scheme. This scheme significantly reduces the computational cost of an approximate solution satisfying the incompressibility constraint but with a diminished accuracy.

Since this last class of methods is widely used, a large number of theoretical and numerical works have been published that discuss their accuracy and the stability properties. The state of the art from both theoretical and numerical points of view is described in the review paper of Guermond et al. [20]. The most widespread methods are pressure-correction schemes developed by Chorin, Temam, Goda and later by Timmermans et al. [7,42,17,43]. They require the solution of two sub-steps for each time step. The pressure is treated explicitly in the first step in order to predict a velocity. Then, by projecting the velocity onto an ad hoc space, the solenoidal velocity and the pressure are computed. The governing equation on the pressure or the pressure increment is a Poisson equation derived from the momentum equation by requiring incompressibility. A less studied alternative method known as the velocity correction scheme, developed by Orszag et al. in [33], Karniadakis et al. in [25], Leriche and Labrosse in [26] and more recently by Guermond and Shen in [21], consists in switching the two sub-steps. All these time-splitting schemes have very similar numerical characteristics, but, numerical evidence show that velocity-correction schemes are more stable compared with pressure-correction schemes. This has been reported with high-order time discretization in [25] and with

* Corresponding author. Address: I2M-Trefle, 16 Avenue Pey-Berland, 66307 Pessac, France. Tel.: +33 (0) 540 006 192; fax: +33 (0) 540 006 668.

E-mail addresses: alexandre.poux@enscbp.fr (A. Poux), glockner@enscbp.fr (S. Glockner), etienne.ahusborde@univ-pau.fr (E. Ahusborde), azaiez@enscbp.fr (M. Azaïez).

0045-7930/$ - see front matter
http://dx.doi.org/10.1016/j.compfluid.2012.08.028

Navier–Stokes equations in [11]. In the latter, the authors propose an unconditionally stable scheme with an original implementation of the inertial term.

The majority of the studies based on these methods consider only the Dirichlet boundary condition. However, in many applications such as free surface problems and channel flows, one also has to deal with an outlet boundary condition which should not disturb upstream flow. A large variety of this kind of boundary condition exists [44,39]. Hereafter we will present some results on the open or traction boundary condition which is efficient for low Reynolds number and fluid–structure interactions [27,8,19]. This boundary condition was successfully used to compute various flows such as those around a circular cylinder, over a backward facing step and in a bifurcated tube [27]. Bruneau and Fabrie proposes, in [6], an evolution of the traction boundary condition involving inertial terms.

With open or traction boundary conditions, to our knowledge, several questions remain open specially when a time splitting method is considered. Indeed, while no studies have been reported with a velocity-correction scheme, a few have been done with pressure correction schemes. Guermond et al., have proven in [20] that only convergence rates between one and 3/2 in space and time for velocity and 1/2 in space and time for the pressure are to be expected with the standard incremental scheme. Févrière et al. in [13] combines the penalty and projection methods to offer better error levels. In [36] we presented an almost second-order accurate version of the boundary condition and pressure-correction scheme. We expect to have the same results with velocity-correction schemes as the two are very similar.

The aim of this paper is to study open boundary conditions using the velocity-correction version of the time splitting methods for the incompressible Navier–Stokes equations. In the first part of this article we describe the governing equations, the velocity-correction schemes and the boundary conditions. Since their numerical properties are independent from the treatment of linearities, we only consider in this part Stokes equations. The usual way to enforce this type of boundary condition on the pressure increment is described along with an improvement we proposed in [36] that gives a satisfactory order of convergence for both pressure and velocity. In a second section, we illustrate numerically the behaviour of the standard methods and the proposed method with a manufactured case with both a finite volume and a spectral Legendre method. Finally, in the last section, we study three physical simulations. In the first, we study the flow over a backward-facing step. In the second, we study the influence of the Reynolds number on the laminar flow structure in a geometry where a bifurcation takes place. In the third, we verify the solution obtained for unsteady flow around a square cylinder.

First of all let us specify some notations. Let us consider a Lipschitz domain $\Omega \subset IR^d$, ($d = 2$ or 3), the generic point of Ω is denoted $\boldsymbol{x}$. The classical Lebesgue space of square integrable functions $L^2(\Omega)$ is endowed with the inner product:

$$(\phi, \psi) = \int_\Omega \phi(\boldsymbol{x})\psi(\boldsymbol{x})\, d\boldsymbol{x}$$

and the norm:

$$\|\psi\|_{L^2(\Omega)} = \left(\int_\Omega |\psi(\boldsymbol{x})|^2 d\boldsymbol{x}\right)^{\frac{1}{2}}.$$

We break the time interval $[0, t^*]$ into N subdivisions of length $\Delta t = \frac{t^*}{N}$, called the time step, and define $t^n = n\Delta t$, for any $n, 0 \leqslant n \leqslant N$. Let $\varphi^0, \varphi^1, \ldots, \varphi^N$ be some sequence of functions in $E = L^2$. We denote this sequence by $\varphi^{\Delta t}$, and we define the following discrete norm:

$$||\varphi^{\Delta t}||_{l^2(E)} = \left(\Delta t \sum_{k=0}^{N} ||\varphi^k||_E^2\right)^{\frac{1}{2}} \tag{1.1}$$

In practice the following error estimator can be used:

$$||\varphi||^2_{E(t^*)} = ||\varphi(\cdot, t^*)||_E \tag{1.2}$$

Finally, bold Latin letters like $\boldsymbol{u}, \boldsymbol{w}, \boldsymbol{f}$, etc., indicate vector valued quantities, while capitals (e.g. $\boldsymbol{X}$, etc.) are functional sets involving vector fields.

2. Governing equations

Let Ω be a regular bounded domain in IR^d with $\boldsymbol{n}$ the unit normal to the boundary $\Gamma = \partial\Omega$ oriented outward and $\boldsymbol{\tau}$ the associated unit tangent vector. We assume that Γ is partitioned into two portions Γ_D and Γ_N. Our study consists, for a given finite time interval $[0, t^*]$ in computing velocity $\boldsymbol{u} = \boldsymbol{u}(\boldsymbol{x}, t)$ and pressure $p = p(\boldsymbol{x}, t)$ fields satisfying:

$$\rho\partial_t\boldsymbol{u} - \mu\Delta\boldsymbol{u} + \nabla p = \boldsymbol{f} \quad \text{in } \Omega\times]0, t^*] \tag{2.3}$$

$$\nabla \cdot \boldsymbol{u} = 0 \quad \text{in } \Omega\times]0, t^*] \tag{2.4}$$

$$\boldsymbol{u} = \boldsymbol{g} \quad \text{on } \Gamma_D\times]0, t^*] \tag{2.5}$$

$$(\mu\nabla\boldsymbol{u} - p\boldsymbol{I}) \cdot \boldsymbol{n} = \boldsymbol{t} \quad \text{on } \Gamma_N\times]0, t^*] \tag{2.6}$$

where ρ and μ are respectively the density and the dynamic viscosity of the fluid and $\boldsymbol{I}$ the unit tensor. The body force $\boldsymbol{f} = \boldsymbol{f}(\boldsymbol{x}, t)$, the constraint $\boldsymbol{t} = \boldsymbol{t}(\boldsymbol{x}, t)$ and the boundary condition $\boldsymbol{g} = \boldsymbol{g}(\boldsymbol{x}, t)$ are known. For the sake of simplicity, we chose $\boldsymbol{g} = \boldsymbol{0}$. Finally, the initial state is characterized by a given $\boldsymbol{u}(\cdot, 0)$.

The boundary condition (2.6) is derived from the pseudo-stress tensor $\tilde{\sigma} = \mu\nabla\boldsymbol{u} - p\boldsymbol{I}$. Considering the Cauchy stress tensor $\sigma = \mu(\nabla\boldsymbol{u} + \nabla^T\boldsymbol{u}) - p\boldsymbol{I}$, one can obtain an alternate traction boundary condition containing the non-symmetrical part:

$$\left(\mu\left(\nabla\boldsymbol{u} + \nabla^T\boldsymbol{u}\right) - p\boldsymbol{I}\right) \cdot \boldsymbol{n} = \boldsymbol{t} \text{ on } \Gamma_N\times]0, t^*] \tag{2.7}$$

As we consider the pseudo-stress tensor in (2.3) and later in (2.16), we will only study here the first one for consistency (which is comonly used, see for exemple [27,20]). Nevertheless, a similar study was carried out with the stress tensor and, since the results are very similar, they are not shown here.

2.1. Velocity-correction schemes for open boundary condition

We shall compute two sequences $(\tilde{\boldsymbol{u}}^n)_{0\leqslant n\leqslant N}$ and $(p^n)_{0\leqslant n\leqslant N}$ in a recurrent way that approximate in some sense the quantities $(\boldsymbol{u}(\cdot, t^n))_{0\leqslant n\leqslant N}$ and $(p(\cdot, t^n))_{0\leqslant n\leqslant N}$, solutions of the unsteady Stokes problem (2.3)–(2.6). The scheme developed by Guermond and Shen (Eqs. (3.6)–(3.8) in [21]) consists of two sub-steps. The first is the prediction problem that computes a pressure increment and a solenoidal velocity: *find* φ^{n+1} and $\boldsymbol{u}^{n+1}$ *such that:*

$$\rho\frac{\alpha\boldsymbol{u}^{n+1} + (\beta - \alpha)\tilde{\boldsymbol{u}}^n + (\gamma - \beta)\tilde{\boldsymbol{u}}^{n-1} - \gamma\tilde{\boldsymbol{u}}^{n-2}}{\Delta t} + \nabla\varphi^{n+1} = \boldsymbol{f}^{\,n+1} - \boldsymbol{f}^{\,n} \quad \text{in } \Omega \tag{2.8}$$

$$\nabla \cdot \boldsymbol{u}^{n+1} = 0 \quad \text{in } \Omega \tag{2.9}$$

$$\boldsymbol{u}^{n+1} \cdot \boldsymbol{n} = 0 \quad \text{on } \Gamma_D \tag{2.10}$$

$$\mu\partial_n(\boldsymbol{u}^{n+1} \cdot \boldsymbol{n}) - p^{n+1} = \boldsymbol{t}^{n+1} \cdot \boldsymbol{n} \quad \text{on } \Gamma_N \tag{2.11}$$

where φ is the pressure increment defined as:

$$\varphi^{n+1} = p^{n+1} - p^n + \chi\mu\nabla \cdot \tilde{u}^n \tag{2.12}$$

The parameter χ is used to switch between the standard incremental scheme ($\chi = 0$) and the rotational one ($\chi = 1$) and parameters α, β, γ depend on the temporal scheme used. Namely:

- $\alpha = 1$, $\beta = -1$, $\gamma = 0$ for the first order Euler time scheme,

- $\alpha = \frac{3}{2}, \beta = -2, \gamma = \frac{1}{2}$ for the second order Backward Difference Formula time scheme.

In practice, this step is processed by solving the following problem: *find* φ^{n+1} *such that:*

$$\nabla\cdot\left(\frac{\Delta t}{\rho}\nabla\varphi^{n+1}\right) = \nabla\cdot\left(\frac{\Delta t}{\rho}(\boldsymbol{f}^{\,n+1}-\boldsymbol{f}^{\,n}) - (\beta-\alpha)\tilde{\boldsymbol{u}}^{n} - (\gamma-\beta)\tilde{\boldsymbol{u}}^{n-1} + \gamma\tilde{\boldsymbol{u}}^{n-2}\right) \quad \text{in } \Omega \tag{2.13}$$

$$\partial_n\varphi^{n+1} = (\boldsymbol{f}^{\,n+1}-\boldsymbol{f}^{\,n})\cdot\boldsymbol{n} \quad \text{on } \Gamma_D \tag{2.14}$$

$$B.C.(\varphi^{n+1}) \quad \text{on } \Gamma_N \tag{2.15}$$

and upgrading the pressure and the solenoidal velocity via (2.12) and (2.8).

The second step is a correction-diffusion problem: *find* $\tilde{\boldsymbol{u}}^{n+1}$ *such that:*

$$\rho\frac{\alpha\tilde{\boldsymbol{u}}^{n+1}+\beta\tilde{\boldsymbol{u}}^{n}+\gamma\tilde{\boldsymbol{u}}^{n-1}}{\Delta t} - \mu\Delta\tilde{\boldsymbol{u}}^{n+1} = \boldsymbol{f}^{\,n+1} - \nabla p^{n+1} \quad \text{in } \Omega \tag{2.16}$$

$$\tilde{\boldsymbol{u}}^{n+1} = \boldsymbol{0} \quad \text{on} \quad \Gamma_D \tag{2.17}$$

$$\mu\partial_n(\tilde{\boldsymbol{u}}\cdot\boldsymbol{n})^{n+1} = \boldsymbol{t}^{n+1}\cdot\boldsymbol{n} + p^{n+1} \quad \text{on } \Gamma_N \tag{2.18}$$

$$\mu\partial_n(\tilde{\boldsymbol{u}}\cdot\boldsymbol{\tau})^{n+1} = t^{n+1}\cdot\boldsymbol{\tau} \quad \text{on } \Gamma_N \tag{2.19}$$

We can note that the solenoidal velocity is the intermediate velocity $\boldsymbol{u}^{n+1}$ and can be totally eliminated from the algorithm while the viscous velocity $\tilde{\boldsymbol{u}}^{n+1}$ obtained at the end of the last step does not satisfy the incompressibility constraint. The velocity-correction scheme, with Dirichlet boundary condition only, has been analyzed among others in [20], and is known to have second order velocity convergence rate in time and, on the pressure convergence rate, from 1 with the standard incremental scheme to 3/2 with the rotational version.

As no numerical or theoretical analysis has been done elsewhere in the literature with this projection method and boundary condition, we are searching in this article for a correct definition of B.C. φ^{n+1}) in (2.15). As usually done in the framework of pressure-correction methods, the standard method consists in the "natural choice" to consider φ^{n+1} equals zero on Γ_N. But, as we observe hereafter, this leads to a kind of numerical locking for $\chi = 0$ since the boundary condition on the pressure increment causes the pressure on the limit to be equal to its initial value. With pressure-correction methods, this problem is known and is usually circumvented by using the rotational incremental version which is also efficient with velocity-correction methods, as our numerical tests illustrate. In [36] we propose a new way to enforce this boundary condition which does not suffer from such problems and which improved the accuracy as it offers optimal convergence rates for the standard incremental pressure-correction scheme while remaining compatible with the rotational one. In the next section, we present an adaptation of this alternative boundary condition and we show afterwards that the same conclusions are to be expected with the velocity-correction scheme.

2.2. Alternative open-boundary condition for the prediction step

In this section we develop the boundary condition on the pressure increment induced by the Hodge-Helmholtz decomposition (2.8). For the sake of simplicity we choose Ω to be a square and we fix Γ_N at its right boundary. The starting point of our approach is the first component of Eq. (2.8). Taking the derivative with respect to x_1, one obtains:

$$\alpha\partial_{x_1}u_{x_1}^{n+1} = \partial_{x_1}\frac{\Delta t}{\rho}\left(f_{x_1}^{n+1} - f_{x_1}^{n} - \partial_{x_1}\varphi^{n+1}\right) - (\beta-\alpha)\partial_{x_1}\tilde{u}_{x_1}^{n} - (\gamma-\beta)\partial_{x_1}\tilde{u}_{x_1}^{n-1} + \gamma\partial_{x_1}\tilde{u}_{x_1}^{n-2} \tag{2.20}$$

Using boundary conditions (2.18) and (2.11) we get:

$$\frac{\alpha}{\mu}(t_{x_1}^{n+1}+p^{n+1}) = \partial_{x_1}\frac{\Delta t}{\rho}\left(f_{x_1}^{n+1}-f_{x_1}^{n}-\partial_{x_1}\varphi^{n+1}\right) - \frac{1}{\mu}\Big((\beta-\alpha)(t_{x_1}^{n}+p^{n}) + \left(\gamma-\beta)(t_{x_1}^{n-1}+p^{n-1}\right) - \gamma(t_{x_1}^{n-2}+p^{n-2})\Big) \tag{2.21}$$

By rearranging terms we obtain:

$$\partial_{x_1}\left(\frac{\Delta t}{\rho}\partial_{x_1}\varphi^{n+1}\right) = \partial_{x_1}\frac{\Delta t}{\rho}\left(f_{x_1}^{n+1}-f_{x_1}^{n}\right) - \frac{1}{\mu}\left(\alpha(p^{n+1}-p^{n}) + \beta(p^{n}-p^{n-1}) + \gamma(p^{n-1}-p^{n-2})\right) - \frac{1}{\mu}\left(\alpha(t_{x_1}^{n+1}-t_{x_1}^{n}) + \beta(t_{x_1}^{n}-t_{x_1}^{n-1}) + \gamma(t_{x_1}^{n-1}-t_{x_1}^{n-2})\right) \tag{2.22}$$

The pressure is replaced with its increment thanks to Eq. (2.12):

$$\partial_{x_1}\left(\frac{\Delta t}{\rho}\partial_{x_1}\varphi^{n+1}\right) = \partial_{x_1}\frac{\Delta t}{\rho}\left(f_{x_1}^{n+1}-f_{x_1}^{n}\right) - \frac{1}{\mu}\big(\alpha(\varphi^{n+1}-\chi\mu\nabla\cdot\tilde{\boldsymbol{u}}^{n}) + \beta(\varphi^{n}-\chi\mu\nabla\cdot\tilde{\boldsymbol{u}}^{n-1}) + \gamma(\varphi^{n-1}-\chi\mu\nabla\cdot\tilde{\boldsymbol{u}}^{n-2})\big) - \frac{1}{\mu}\left(\alpha(t_{x_1}^{n+1}-t_{x_1}^{n}) + \beta(t_{x_1}^{n}-t_{x_1}^{n-1}) + \gamma(t_{x_1}^{n-1}-t_{x_1}^{n-2})\right) \tag{2.23}$$

In order to simplify the expressions, we define the known quantity H^{n+1}:

$$H^{n+1} = \chi\nabla\cdot(\alpha\tilde{\boldsymbol{u}}^{n}+\beta\tilde{\boldsymbol{u}}^{n-1}+\gamma\tilde{\boldsymbol{u}}^{n-2}) - \frac{1}{\mu}(\beta\varphi^{n}+\gamma\varphi^{n-1}) - \frac{1}{\mu}\left(\alpha(t_{x_1}^{n+1}-t_{x_1}^{n}) + \beta(t_{x_1}^{n}-t_{x_1}^{n-1}) + \gamma(t_{x_1}^{n-1}-t_{x_1}^{n-2})\right) \tag{2.24}$$

The Eq. (2.23) can be rewritten as:

$$\left(\partial_{x_1}\frac{\Delta t}{\rho}\partial_{x_1} + \frac{\alpha}{\mu}\right)\varphi^{n+1} = \partial_{x_1}\frac{\Delta t}{\rho}\left(f_{x_1}^{n+1}-f_{x_1}^{n}\right) + H^{n+1} \tag{2.25}$$

Subtracting (2.24) in (2.13) leads to a version that is easier to implement:

$$\left(\partial_{x_2}\frac{\Delta t}{\rho}\partial_{x_2} - \frac{\alpha}{\mu}\right)\varphi^{n+1} = \partial_{x_2}\frac{\Delta t}{\rho}\left(f_{x_2}^{n+1}-f_{x_2}^{n}\right) - \nabla\cdot\big((\beta-\alpha)\tilde{\boldsymbol{u}}^{n} + (\gamma-\beta)\tilde{\boldsymbol{u}}^{n-1} - \gamma\tilde{\boldsymbol{u}}^{n-2}\big) - H^{n+1} \tag{2.26}$$

One interesting thing in this version, is that it only involves the tangential derivative of φ which permits the boundary equation to be uncoupled from the rest of the domain. Thus, it is possible to solve this equation independently in a previous step, and use the solution φ^* as a non-homogeneous Dirichlet boundary condition during the prediction step.

To conclude this section, we explicit the full time-splitting algorithm in the presence of open boundary conditions in a three dimensional Cartesian domain. Denoting $\boldsymbol{n}, \boldsymbol{\tau}_1$ and $\boldsymbol{\tau}_2$ respectively the units normal to the boundary oriented outward and the two associated tangent vectors, and $\boldsymbol{\tau}$ the units normal to $\partial\Gamma_N$, we have:

Compute quantity H^{n+1}:

$$H^{n+1} = \chi\nabla\cdot(\alpha\tilde{\boldsymbol{u}}^{n}+\beta\tilde{\boldsymbol{u}}^{n-1}+\gamma\tilde{\boldsymbol{u}}^{n-2}) - \frac{1}{\mu}(\beta\varphi^{n}+\gamma\varphi^{n-1}) - \frac{1}{\mu}\left(\alpha(t_{n}^{n+1}-t_{n}^{n}) + \beta(t_{n}^{n}-t_{n}^{n-1}) + \gamma(t_{n}^{n-1}-t_{n}^{n-2})\right) \tag{2.27}$$

Boundary condition step: *find* φ^* *such that:* (Eq. (2.29) comes from Eq. (2.14))

$$\left(\partial_{\tau_1}\frac{\Delta t}{\rho}\partial_{\tau_1}+\partial_{\tau_2}\frac{\Delta t}{\rho}\partial_{\tau_2}-\frac{\alpha}{\mu}\right)\varphi^* = \partial_{\tau_1}\frac{\Delta t}{\rho}\left(f^{n+1}_{\tau_1}-f^{n}_{\tau_1}\right)+\partial_{\tau_2}\frac{\Delta t}{\rho}\left(f^{n+1}_{\tau_2}-f^{n}_{\tau_2}\right) - \nabla\cdot\left((\beta-\alpha)\tilde{\boldsymbol{u}}^n+(\gamma-\beta)\tilde{\boldsymbol{u}}^{n-1}-\gamma\tilde{\boldsymbol{u}}^{n-2}\right)-H^{n+1}\quad \text{on } \Gamma_N \tag{2.28}$$

$$\partial_\tau\varphi^* = \left(f^{n+1}_{\tau}-f^{n}_{\tau}\right)\quad \text{on } \partial\Gamma_N \tag{2.29}$$

Prediction step: *find* φ^{n+1} *such that:*

$$\nabla\cdot\left(\frac{\Delta t}{\rho}\nabla\varphi^{n+1}\right) = \nabla\cdot\left(\frac{\Delta t}{\rho}(\boldsymbol{f}^{\,n+1}-\boldsymbol{f}^{\,n})-(\beta-\alpha)\tilde{\boldsymbol{u}}^n-(\gamma-\beta)\tilde{\boldsymbol{u}}^{n-1}+\gamma\tilde{\boldsymbol{u}}^{n-2}\right)\quad \text{in } \Omega \tag{2.30}$$

$$\partial_n\varphi^{n+1} = \left(\boldsymbol{f}^{\,n+1}-\boldsymbol{f}^{\,n}\right)\cdot\boldsymbol{n}\quad \text{on} \Gamma_D \tag{2.31}$$

$$\varphi^{n+1}=\varphi^*\quad \text{on } \Gamma_N \tag{2.32}$$

Compute the updated pressure and the divergence-free velocity via:

$$p^{n+1}=p^n+\varphi^{n+1}-\chi\mu\nabla\cdot\tilde{\boldsymbol{u}}^n\quad \text{in } \Omega \tag{2.33}$$

$$\alpha\boldsymbol{u}^{n+1}=\frac{\Delta t}{\rho}(\boldsymbol{f}^{\,n+1}-\boldsymbol{f}^{\,n}-\nabla\varphi^{n+1})-(\beta-\alpha)\tilde{\boldsymbol{u}}^n -(\gamma-\beta)\tilde{\boldsymbol{u}}^{n-1}+\gamma\tilde{\boldsymbol{u}}^{n-2}\quad \text{in } \Omega \tag{2.34}$$

Correction-diffusion problem: *find* $\tilde{\boldsymbol{u}}^{n+1}$ *such that:*

$$\rho\frac{\alpha\tilde{\boldsymbol{u}}^{n+1}+\beta\tilde{\boldsymbol{u}}^n+\gamma\tilde{\boldsymbol{u}}^{n-1}}{\Delta t}-\mu\Delta\tilde{\boldsymbol{u}}^{n+1}=\boldsymbol{f}^{\,n+1}-\nabla p^{n+1}\quad \text{in } \Omega \tag{2.35}$$

$$\tilde{\boldsymbol{u}}^{n+1}=\boldsymbol{0}\quad \text{on } \Gamma_D \tag{2.36}$$

$$\left(\mu\nabla\tilde{\boldsymbol{u}}^{n+1}-p^{n+1}\boldsymbol{Id}\right)\cdot\mathbf{n}=\boldsymbol{t}^{n+1}\quad \text{on } \Gamma_N \tag{2.37}$$

The choice of χ permits us to switch from the standard incremental scheme ($\chi = 0$) to the rotational form ($\chi = 1$) while the values of α, β, γ move from the first time order to the second:

- $\alpha = 1$, $\beta = -1$, $\gamma = 0$ for first order Euler time scheme,
- $\alpha=\frac{3}{2}, \beta=-2, \gamma=\frac{1}{2}$ for second order Backward Difference Formula time scheme.

3. Numerical experiments

To assess the accuracy of our method, we perform convergence tests with finite volume and spectral Legendre methods [10]. We start this section by giving a brief description of the two spatial discretizations and tools for the numerical simulations. Then, numerical experiments involving the open boundary conditions are separated into two verification cases on manufactured solutions of the Stokes equations on the different boundary conditions, and two validations on physical cases governed by the Navier–Stokes equations.

3.1. Spatial discretization and linear solvers

3.1.1. Finite volume case

To avoid the well known spurious modes phenomena, the correction step uses the stable finite volume staggered grid of the Marker and Cells type [22]. The approximation of the prediction-diffusion of the Stokes problem step uses a centered scheme of second order to compute the predicted velocity. All the computations are made using the parallel version of a Navier–Stokes solver based on the block-structured mesh partitioner described in [1]. Finally, in order to solve the linear systems we use:

- For the prediction step, the multi frontal sparse direct solver MUMPS [2] for manufactured cases or the GMRES method with a semi-coarsening geometric multi-grid preconditioner [40,5] of the HYPRE library [24] for physical cases.
- For the correction step, the iterative BiCGStab method with a point Jacobi preconditioner of the HYPRE library.

3.1.2. Spectral Legendre case

Ω is considered as the union of quadrangular elements $\overline{\Omega}=\cup_{k=1}^{K}\overline{\Omega}_k$. For simplification, we consider only rectilinear elements with edges collinear to the axes x and y, that is:

$\Omega_k =]c_k, c_{k'}[\times]d_k, d_{k'}[$

The partition is conforming in the sense that the intersection of two adjacent elements is either a vertex, a whole edge, or a whole face. The discrete and stable subspaces to approximate the velocity and the pressure, $\boldsymbol{X}_p\subset(H^1_0(\Omega))^2$ and $M_p\subset L^2_0(\Omega)$ are chosen to be:

$$\boldsymbol{X}_p=\left\{\boldsymbol{w}_p\in(H^1_0(\Omega))^2, \forall k=1,\ldots,K,\quad \boldsymbol{w}^k_p=\boldsymbol{w}_{p|\Omega_k}\in(P_p(\Omega))^2\right\} \tag{3.38}$$

$$M_p=\left\{q_p\in L^2(\Omega), \forall k=1,\ldots,K,\quad q^k_p=q_{p|\Omega_k}\in P_{p-2}(\Omega_k),\quad \int_\Omega q_p\, d\boldsymbol{x}=0\right\} \tag{3.39}$$

The spectral Legendre approach consists in using the Legendre–Galerkin methods introduced in [10] applied to the variational formulation of elliptic problems introduced in our algorithms.

3.2. Numerical results for the Stokes problem

To evaluate the accuracy of the scheme, we present hereafter two convergence studies on a manufactured test case: firstly with the standard implementation of the open boundary condition ($\varphi = 0$) and secondly with the proposed one ($\varphi=\varphi^*$). The error estimator $||\varphi||^2_{L^2(t^*)}$ defined in (1.2) is used against the pressure p^{n+1} and the final velocity $\tilde{\boldsymbol{u}}^{n+1}$. The domain is chosen to be $\Omega=[-1,1]^2$ and we enforce the open boundary condition on the right part of the box and a Dirichlet boundary condition everywhere else. Exact solutions for $\boldsymbol{u}^{ex}=\left(u^{ex}_{x_1},u^{ex}_{x_2}\right)$ and p^{ex} are:

$$u^{ex}_{x_1}(x_1,x_2,t)=\sin(x_1)\sin(x_2)\cos(2\pi\omega t)$$
$$u^{ex}_{x_2}(x_1,x_2,t)=\cos(x_1)\cos(x_2)\cos(2\pi\omega t)$$
$$p^{ex}(x_1,x_2,t)=-2\cos(1)\sin(2(x_1-1)-x_2)\cos(2\pi\omega t)$$

3.2.1. The standard open boundary condition

3.2.1.1. Error convergence rate in space. In order to study the spatial splitting error we carried out the first numerical experiment with $\omega=0$. The time step is fixed at $\Delta t=10^{-3}$ and we run the algorithm for different values of Δx. Stationary tolerance is set to 10^{-12}.

Finite volume case

As long as we attempt to approximate exact solutions by a second order scheme, we expect that the errors decay like Δx^2, but we show in Fig. 1 that spatial convergence rates are limited to one for velocity and to 1/2 for pressure with the standard version in which $\varphi = 0$ is enforced on the boundary condition. The usual way to overcome this difficulty with pressure-correction methods, where the same problem is encountered, consists in switching to the rotational formulation. This solution also works in the framework of velocity-correction methods as it gives a second order convergence rate on the velocity and the pressure.

Spectral Legendre case

As we approximate the same solution by high degree polynomials it is well known that the convergence rate is expected to become of exponential order, meaning that the errors decay like C^p with $C\in]0,1[$. However, as for the finite volume approximation, for the standard version we observe a saturation of the error rate for both velocity and pressure. The saturation level is large enough to be regarded as a convergent state. Again, the rotational

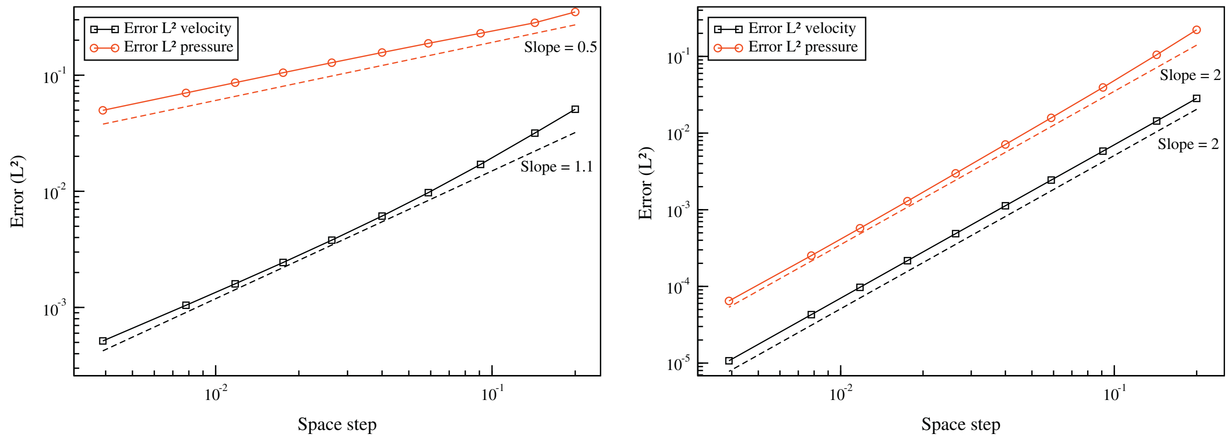

Fig. 1. Spatial convergence rates with the standard incremental scheme (left) and the rotational scheme (right) with $\Delta t = 10^{-3}$ with standard open boundary conditions and finite volume method.

version solves the problem and allows spectral convergence. Fig. 2 shows the relative error, on a semi-logarithmic scale as a function of p.

3.2.1.2. Error convergence rate in time. To study the time splitting error, we consider the unsteady case $\omega = 0.7$ and the errors (1.2) at $t^* = 1$ with a second order time discretization for a range of time steps $5 \times 10^{-4} \leqslant \Delta t \leqslant 10^{-1}$.

With the finite volume method, we fixed Δx at 1/256 and plotted the errors in Fig. 3. The time convergence rate on the velocity is around 3/2, and on the pressure: 1/2 with standard incremental scheme and 1 with the rotational one.

With spectral Legendre case, we fixed a number of elements $K = 1$ and polynomial degree p fixed at 18 and plotted the errors in Fig. 4. The standard incremental scheme gives worst results with no convergence at all for either velocity or pressure. With the rotationnal scheme, we obtain the same convergence rate as with the finite volume method.

3.2.2. The proposed open boundary condition

3.2.2.1. Error convergence rate in space. With the proposed boundary condition, the representative curves of Figs. 5 and 6 show that in the stationary case the spatial convergence rate of the velocity and the pressure are optimal with the standard ($\chi = 0$) and the rotational ($\chi = 1$) form with the errors decaying like Δx^2 for finite volume and C^p with $C \in]0, 1[$ for spectral Legendre.

3.2.2.2. Error convergence rate in time. The representative curves of Fig. 7 show that, with the finite volume method, we have a convergence rate of two for the velocity and 3/2 for pressure with the standard incremental scheme and two with the rotational one for both velocity and pressure. Thus, the convergence rate in the presence of an open boundary condition is now brought to the level observed with the Dirichlet boundary condition.

With spectral Legendre methods, we can see in Fig. 8 that we also ensure a second order convergence rate for the velocity. But, unlike the finite volume case for which the rotational and standard versions give the same results, with slight improvement for the benefit of the first, the numerical results from spectral Legendre method show a distinct advantage for the standard version. This conclusion is confirmed by several numerical tests. A similar conclusion can be found in the paper of Guermond and Shen [21] where the Dirichlet boundary condition is considered for the Stokes problem (on the right part of figure [3]).

3.2.3. Discussions

The spatial convergence study leads us to the following conclusion. While the standard incremental scheme offers an optimal convergence rate with Dirichlet boundary conditions, the standard open boundary condition limits the convergence rates to 1 for the velocity and 1/2 for pressure with finite volume method and does not give spectral convergence with spectral Legendre. This numerical locking can be avoided with the rotational incremental scheme. However, the proposed method provides an optimal con-

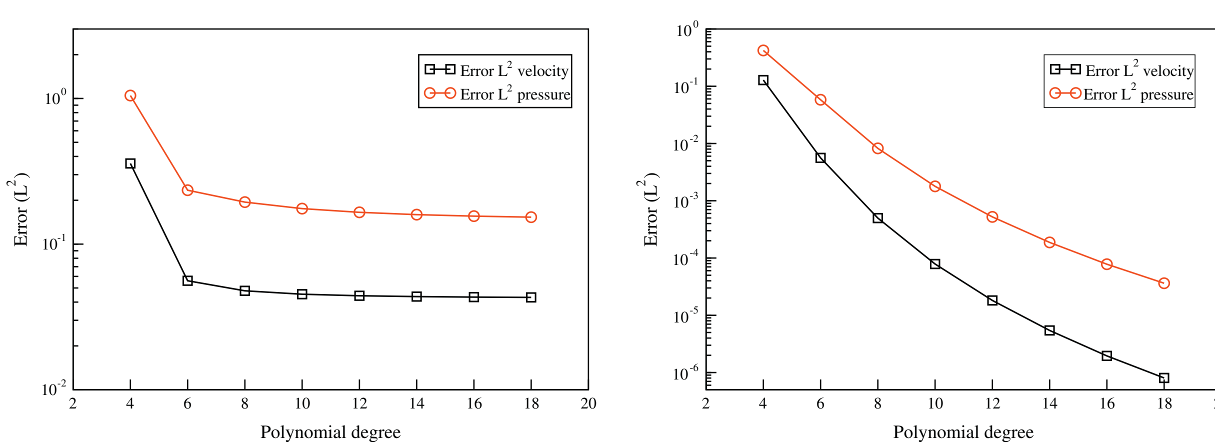

Fig. 2. Spatial convergence rates with the standard incremental scheme (left) and the rotational scheme (right) with $\Delta t = 10^{-3}, K = 1$ and $p = 18$ with standard open boundary conditions and spectral Legendre method.

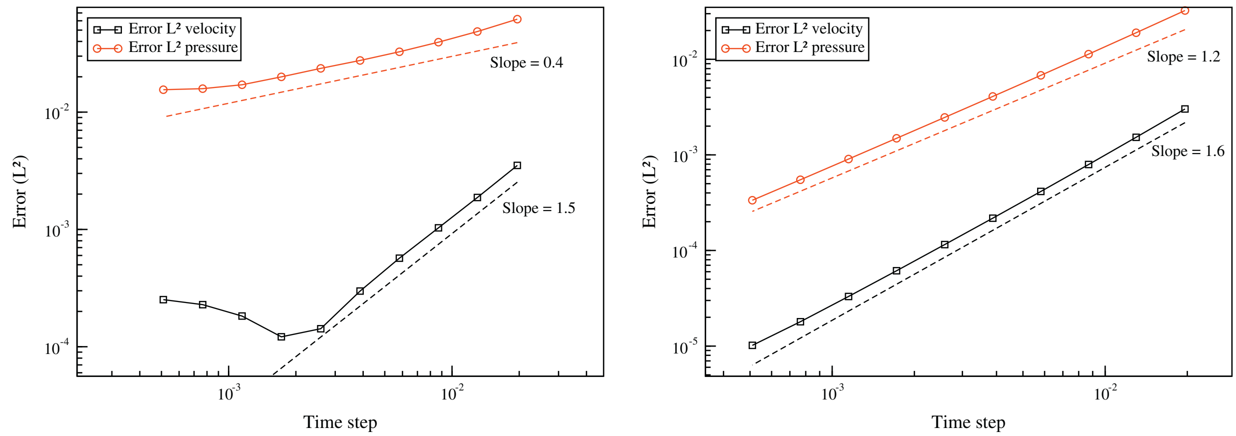

Fig. 3. Time convergence rates with the standard incremental scheme (left) and the rotational scheme (right) at $t^* = 1$ with $\Delta x = 1/256$ with standard open boundary conditions and finite volume method.

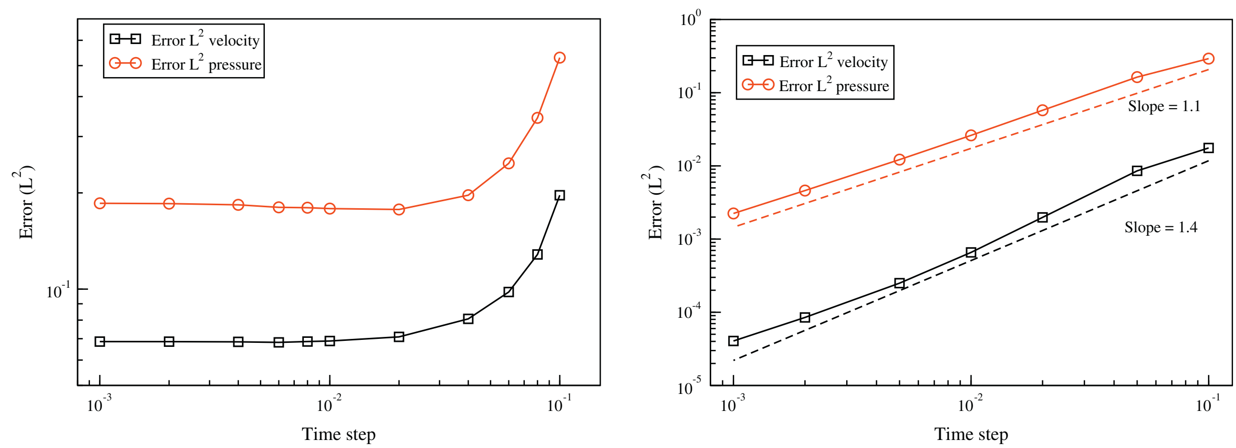

Fig. 4. Time convergence rates with the standard incremental scheme (left) and the rotational scheme (right) at $t^* = 1$ with $K = 1$ and $p = 18$ with standard open boundary conditions and spectral Legendre method.

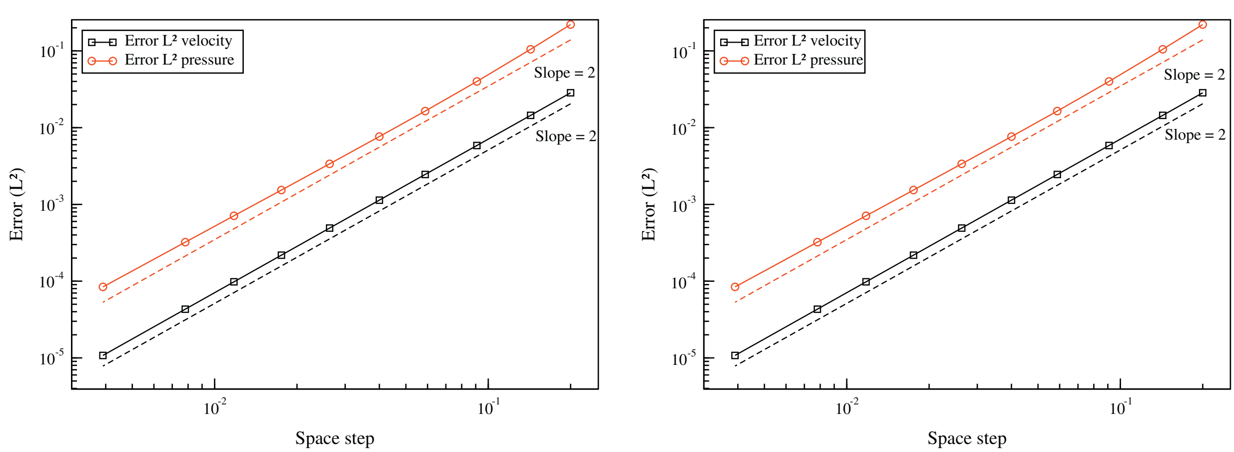

Fig. 5. Spatial convergence rates with the standard incremental scheme (left) and the rotational scheme (right) with $\Delta t = 10^{-3}$ with proposed open boundary conditions and finite volume method.

vergence rate in space in the standard ($\chi = 0$) and the rotational ($\chi = 1$) form.

About the error convergence rate in time, we can say that the standard scheme is limited to a first order convergence rate for the velocity and 1/2 for the pressure while the proposed implementation yields a second order convergence rate for the velocity and 3/2 for pressure which are exactly the convergence rates obtained with Dirichlet boundary conditions only. The rotational scheme improves the proposed open boundary condition to a second order convergence rate for velocity and pressure, but this is not the case with the standard open boundary condition which remains at 3/2 for the velocity and one for the pressure.

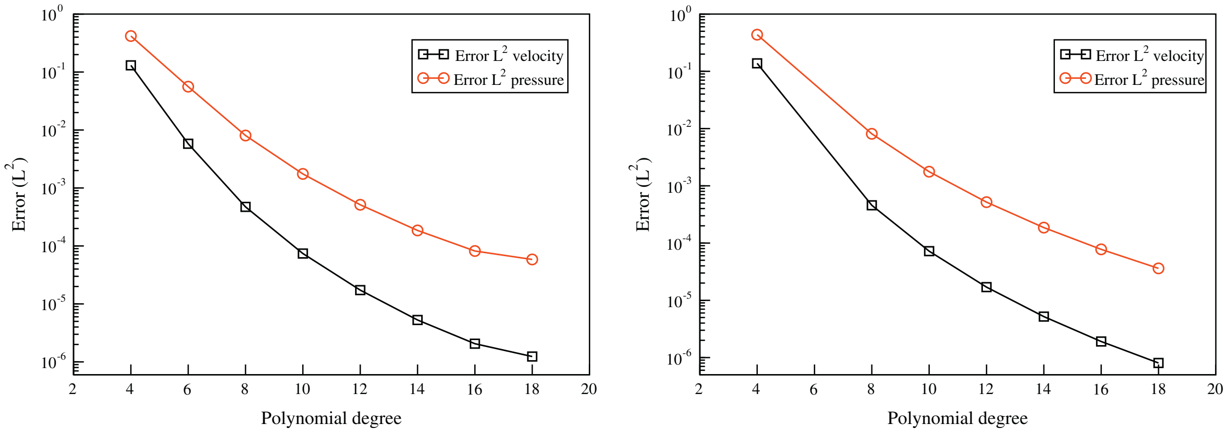

Fig. 6. Spatial convergence rates with the standard incremental scheme (left) and the rotational scheme (right) with $\Delta t = 10^{-3}, K = 1$ and $p = 18$ with proposed open boundary conditions and spectral Legendre method.

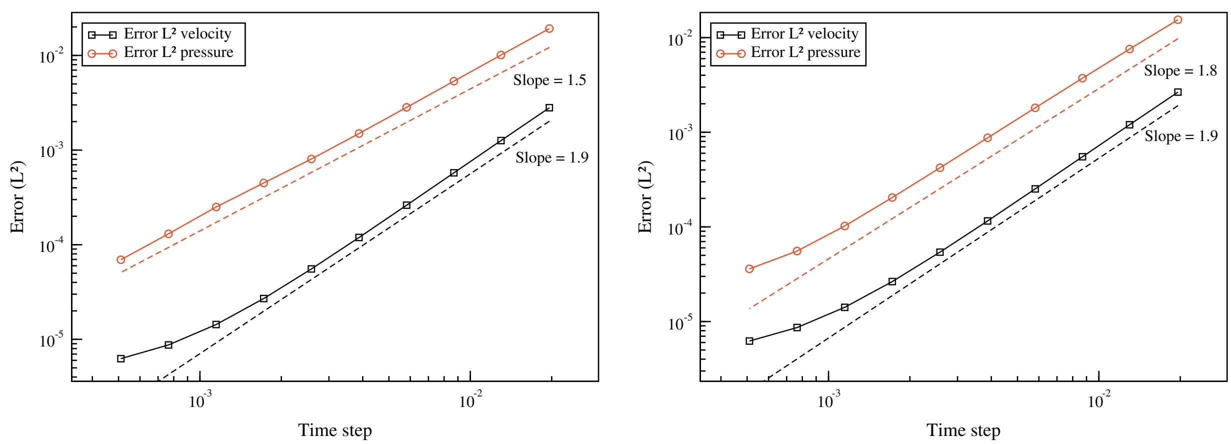

Fig. 7. Time convergence rates with the standard incremental scheme (left) and the rotational scheme (right) at $t^* = 1$ with $\Delta x = 1/256$ with the proposed open boundary conditions and finite volume method.

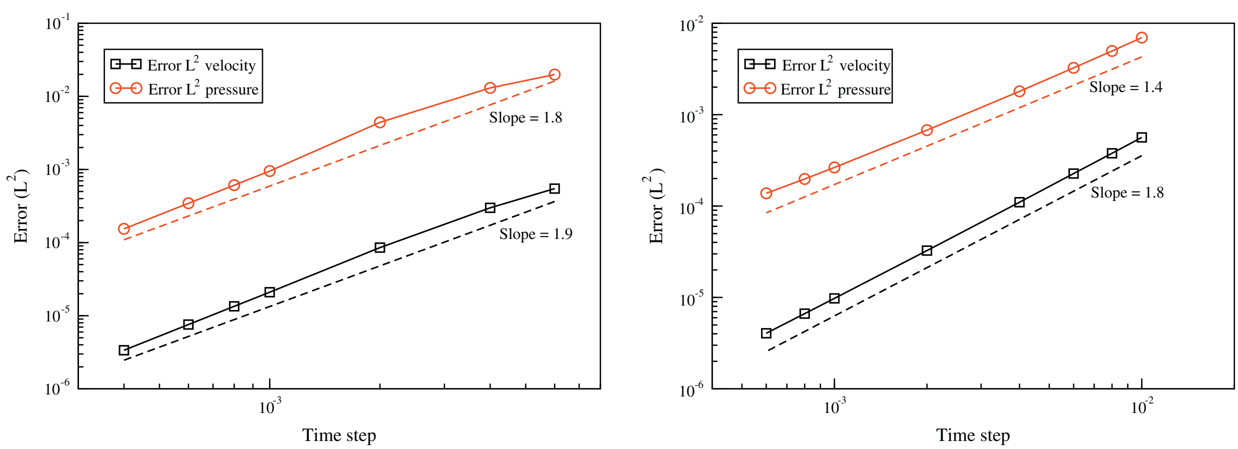

Fig. 8. Time convergence rates with the standard incremental scheme (left) and the rotational scheme (right) at $t^* = 1$ with $K = 1$ and $p = 18$ with the proposed open boundary conditions and spectral Legendre method.

Finally, with the finite volume method, we observe in all computations that $\nabla \cdot \boldsymbol{u}^{n+1} = 0$ is reached at the computational precision (10^{-14}) inside the domain. However, with the standard implementation of the open boundary condition, the incompressibility constraint is not verified at the boundary condition whereas it is with the proposed boundary condition. With the spectral Legendre method the constraint is not exactly satisfied which is due to spatial discretization.

Remark 1. In Figs. 7 and 3 (left) there is saturation of the time error by the space error at small time steps due to space discretization being too coarse.

Remark 2. A similar study was carried out with the open boundary condition (homogeneous or not); the norm $||\varphi^{\Delta t}||_{l^2(E)}$ (see 1.1) was also used. Since the results lead to the same conclusions, they are not shown here.

Remark 3. In the framework of pressure-correction schemes, Guermond et al. proved in [19] that, for stability issues, χ is necessarily strictly less than $2\mu/d$ for pressure-correction schemes. However, with velocity-correction schemes, this seems to be unnecessary.

Remark 4. We note that with the finite volume method the scheme is stable for any Δt, but for $\Delta t < \Delta x^2$ the error is nearly constant as illustrated in Fig. 9. However, with the spectral Legendre method, the scheme is unstable when $\Delta t < p^{-2}$.

3.3. Numerical results for the Navier–Stokes flows

In order to validate the code, we study hereafter the flow over a backward-facing step, studied in [15,4,28,12,18], the steady flow in a bifurcated tube we studied in [27,36] and the unsteady flow past a square section cylinder [23,35,41,32,34,36]. We show that we obtain similar results as in [15,28] for the backward-facing step case and, in both two other cases, we obtain the same results as in [36]. We also develop the bifurcation case by studying the effect of the Reynolds number on the structure of the flow.

The rotational scheme is used with finite volume method and second order time discretization presented in a previous section. The approach adopted for the treatment of the Navier–Stokes non-linear term $(\boldsymbol{u}\cdot\nabla)\boldsymbol{u}$ involved in the material derivative of the velocity consists in incorporating it in the correction-diffusion step and linearizing it by $((2\tilde{\boldsymbol{u}}^n - \tilde{\boldsymbol{u}}^{n-1})\cdot\nabla)\tilde{\boldsymbol{u}}^{n+1}$ and applying a second-order centered scheme on its conservative form.

3.3.1. Flow over a backward-facing step

We consider the two dimensional steady flow over a backward-facing step at $Re = 800$ studied by Garling in [15], Gresho et al. in [18], Barton in [4], Lyn in [28] and more recently by Erturk in [12]. In order to compare our results with those from [15,28], we choose not to consider the inlet part of the step. Hence, we deal with the Navier–Stokes equations set on a purely rectangular domain $\Omega = [0,30]\times[-0.5,0.5]$.

The left boundary condition at $\{x_1 = 0\}$ is separated in two parts. In the bottom $\{-0.5 < x_2 < 0\}$ there is a no slip condition (the step). The upper one $\{0 < x_2 < 0.5\}$ is a Dirichlet boundary set to Poiseuille flow with a unitary flow rate. The outflow boundaries at $\{x_1 = 30\}$ is the proposed open boundary condition, the remaining boundaries being the no-slip condition. Initialization is made with $\boldsymbol{u}^0 = \boldsymbol{0}$ and $p^0 = 0$.

Fig. 10 shows steady state for $Re = 800$ based on the height of the channel ($\rho = 1$ kg m^{-3} and $\nu = 1/800$ m s^{-2}). The flow is composed of three eddies. A first one is attached to the lower wall (B) and a second one is attached to the upper horizontal wall (A). The last one is a Moffatt ([31]) corner vortice (C) appearing in the lower left corner due to the sudden expension of the section.

We compute two parameters characterizing the flow:

- The total kinetic energy: $e_c = \int_\Omega \frac{1}{2}\rho\boldsymbol{u}^2\, d\boldsymbol{x}$
- The charge drop: $\Delta h = \frac{1}{2}\left[\int_L (\boldsymbol{u}\cdot\boldsymbol{n})^2\, dl - \int_R (\boldsymbol{u}\cdot\boldsymbol{n})^2\, dl\right] + \frac{1}{\rho}\left[\int_L p\, dl - \int_R p\, dl\right]$

where L is the left boundary condition, and R right one.

The Richardson extrapolation framework [37,38] is used to compute the convergence rates and extrapolated values of these parameters computed on four meshes of step size h_1, h_2, h_3 and h_4 verifying consecutive ratio equal to two. The convergence rate α and the extrapolated value f_{ext} with four meshes are given by:

$$\alpha = \frac{\ln\left(\frac{f_{h_1} - f_{h_3}}{f_{h_2} - f_{h_4}}\right)}{\ln\left(\frac{h_1}{h_2}\right)} \tag{3.40}$$

$$f_{\mathrm{ext}} = \frac{\left(\frac{h_3}{h_4}\right)^\alpha f_{h_4} - f_{h_3}}{\left(\frac{h_3}{h_4}\right)^\alpha - 1} \tag{3.41}$$

We assess the accuracy of the solutions by computing the parameters for three meshes, the convergence rates and the extrapolated values. The results are detailed in Table 1 and illustrated in the Fig. 11 where one can see that a second order space convergence rate is obtained.

In order to precisely compare the results with [15,28], a description of the eddies (position (x_1, x_2) and vorticity (ω) at the center, and detachment and reattachment points coordinates) is given in Table 2. We observe that the results are very close to those obtained in [15] with a finite elements method and those obtained in [28] with a spectral method. In both cases an open boundary condition has also been used, except that Gartling set the tangential velocity to zero in [15].

We can also compare the pressure and shear stress distribution on the upper and lower wall as illustrated in the Fig. 12 and the cross-channel profiles at $x = 7$ and $x = 15$ of the velocity, vorticity, pressure, normal and shear stress in Figs. 13–15. One can see that we are in total agreement with the reference [15].

In the Figs. 12–15 we referenced each local extremum with numbers. Following a procedure detailed in [29,30], it is possible to compute convergence order and extrapolation of the values and positions of some of them. The reason why its not possible on all extrema is due to the fact that profiles from two disctinct meshes may intersect in the vicinity of an extrema. First the profiles of the three coarserst meshes are interpolated on the nodes of the finest grid using a cubic spline interpolation. Then, on each node, we can proceed to Richardson extrapolation. At last, the extrapolated profiles are interpolated on a finer grid to obtain more precise positions and values of the extremum. Results are detailed in Table 3.

3.3.2. Flow in a bifurcated tube

We deal with the Navier–Stokes equations set on the domain shown in Fig. 16:

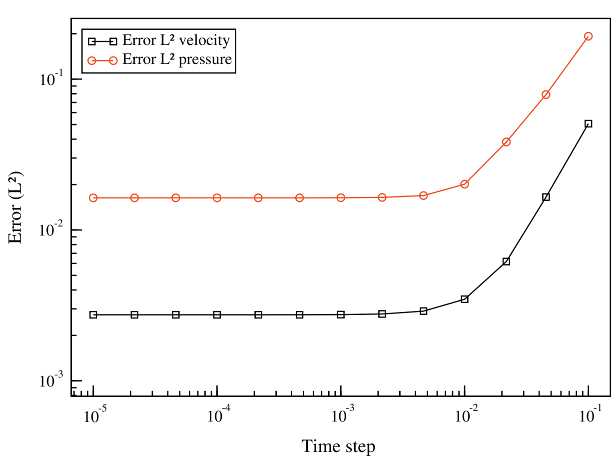

Fig. 9. Time convergence with the standard incremental scheme at $t^* = 1$ with $\Delta x = 1/10$ with the proposed open boundary conditions.

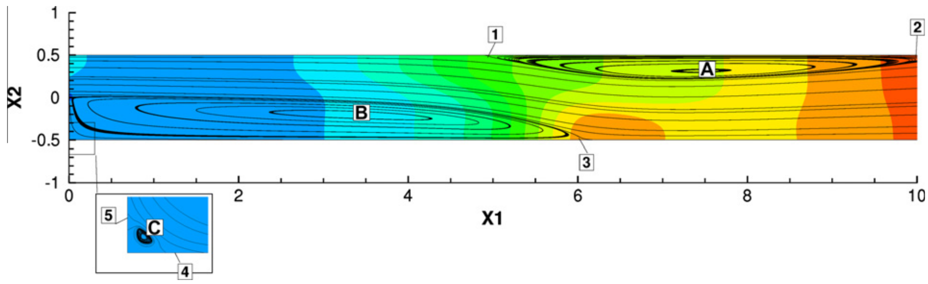

Fig. 10. Steady state of the backward-facing step case at Reynolds number equal to 800. Pressure and streamlines. Eddies are highlighted with letters, detachment and reattachment points are numbered.

Table 1
Details of some parameters in the backward-facing step case for different meshes. Convergence rates and extrapolated values.

Space step size	1/50	1/100	1/200	1/400	Extrapolation	
					Value	Order
Kinetic energy	$5.6148 \times 10^{+0}$	$5.6228 \times 10^{+0}$	$5.6248 \times 10^{+0}$	$5.6253 \times 10^{+0}$	$5.6255 \times 10^{+0}$	2.00
Charge drop	-7.8764×10^{-2}	-7.9092×10^{-2}	-7.9183×10^{-2}	-7.9213×10^{-2}	-7.9225×10^{-2}	1.80

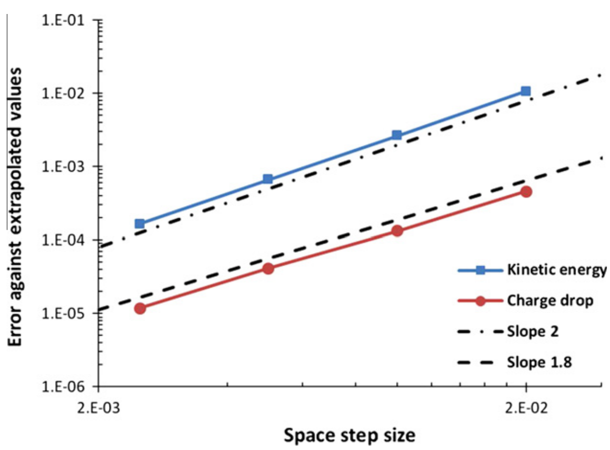

Fig. 11. Spatial convergence rate based on the extrapolation.

$$\Omega = [0, 8] \times [-0.5, 0.5] \setminus \{[0, 0.5] \times [-0.5, 0] \cup [1.5, 8] \times [-0.1, 0.2]\}$$

The inflow boundary at $\{x_1 = 0\}$ is a Dirichlet boundary set to Poiseuille flow with a unitary flow rate. The two outflow boundaries at $\{x_1 = 8\}$ are the proposed open boundary condition, the remaining boundaries being the no-slip condition. Initialization is made with $\boldsymbol{u}^0 = \boldsymbol{0}$ and $p^0 = 0$.

Fig. 16 shows steady state for $Re = 600$ based on the height of the larger section ($\rho = 1\ \mathrm{kg\ m^{-3}}$ and $\nu = 1/600\ \mathrm{m\ s^{-2}}$). The flow is composed of six eddies. An infinite series of Moffatt ([31]) corner vortices (D, E, F) of increasingly smaller amplitude appears in the lower left corner due to the sudden expansion of the section. Three other recirculations (A, B, C) are attached to the horizontal walls due to the contraction of the section.

In order to characterize the flow, we compute the total kinetic energy, the outflux and the charge drops in the upper or lower channel. The Richardson extrapolation framework [37,38] (Eqs. (3.40), (3.41)) continue to be used to compute the convergence rates and extrapolated values.

In order to precisely compare the results with [36], the values at $Re = 600$ of the parameters for five meshes are detailed in Table 4 and the convergence rates computed with the four finest meshes in Tables 5. A description of the eddies (position (x_1, x_2) and vorticity (ω) at the center, and detachment and reattachment points coordinates) is given in Table 6. We observe that the results are qualitatively the same as in [27], where an open boundary condition has also been used, and very close to those we described in

Table 2
Details of eddies characteristics in the the backward-facing step case for different meshes.

Δx	0.02	0.01	0.005	0.0025	Gartling [15]	Lyn [28]
Eddy A x_1	$7.4510 \times 10^{+0}$	$7.4514 \times 10^{+0}$	$7.4513 \times 10^{+0}$	$7.4551 \times 10^{+0}$	$7.400 \times 10^{+0}$	$7.4470 \times 10^{+0}$
Eddy A x_2	3.1411×10^{-1}	3.1510×10^{-1}	3.1528×10^{-1}	3.1535×10^{-1}	3.000×10^{-1}	3.1500×10^{-1}
Eddy A ω	$1.1784 \times 10^{+0}$	$1.1511 \times 10^{+0}$	$1.1509 \times 10^{+0}$	$1.1493 \times 10^{+0}$	$1.322 \times 10^{+0}$	$1.3212 \times 10^{+0}$
Point 1 x_1	$4.9800 \times 10^{+0}$	$4.9250 \times 10^{+0}$	$4.8900 \times 10^{+0}$	$4.8725 \times 10^{+0}$	$4.850 \times 10^{+0}$	$4.8534 \times 10^{+0}$
Point 2 x_1	$1.0280 \times 10^{+1}$	$1.0400 \times 10^{+1}$	$1.0440 \times 10^{+1}$	$1.0461 \times 10^{+1}$	$1.048 \times 10^{+1}$	$1.0479 \times 10^{+1}$
Eddy B x_1	$3.3861 \times 10^{+0}$	$3.3932 \times 10^{+0}$	$3.3953 \times 10^{+0}$	$3.3958 \times 10^{+0}$	$3.350 \times 10^{+0}$	$3.3920 \times 10^{+0}$
Eddy B x_2	-2.0362×10^{-1}	-2.0411×10^{-1}	-2.0421×10^{-1}	-2.0425×10^{-1}	-2.000×10^{-1}	-2.0400×10^{-1}
Eddy B ω	$-2.2639 \times 10^{+0}$	$-2.2602 \times 10^{+0}$	$-2.2622 \times 10^{+0}$	$-2.2621 \times 10^{+0}$	$-2.283 \times 10^{+0}$	$-2.2822 \times 10^{+0}$
Point 3 x_1	$6.0300 \times 10^{+0}$	$6.0700 \times 10^{+0}$	$6.0850 \times 10^{+0}$	$6.0913 \times 10^{+0}$	$6.100 \times 10^{+0}$	$6.0964 \times 10^{+0}$
Eddy C x_1	3.0233×10^{-2}	3.3770×10^{-2}	3.4744×10^{-2}	3.4847×10^{-2}	–	–
Eddy C x_2	-4.7002×10^{-1}	-4.6653×10^{-1}	-4.6553×10^{-1}	-4.6455×10^{-1}	–	–
Eddy C ω	3.3173×10^{-3}	5.6241×10^{-3}	6.2840×10^{-3}	6.3700×10^{-3}	–	–
Point 4 x_1	6.0000×10^{-2}	7.0000×10^{-2}	8.0000×10^{-2}	8.3750×10^{-2}	–	–
Point 5 x_2	4.4000×10^{-1}	4.3000×10^{-1}	4.2500×10^{-1}	4.2000×10^{-1}	–	–

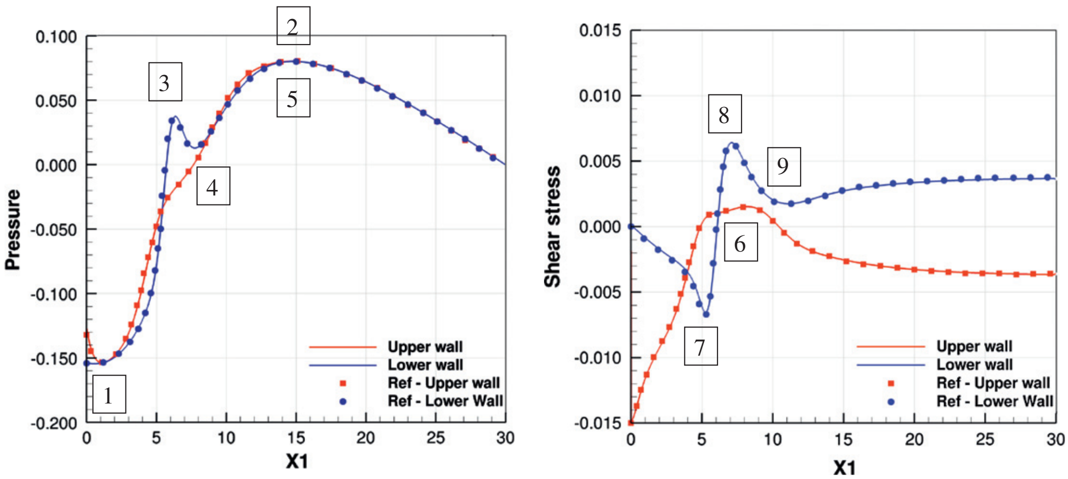

Fig. 12. Pressure and shear stress along upper and lower channel wall. Ref. from Gartling [15].

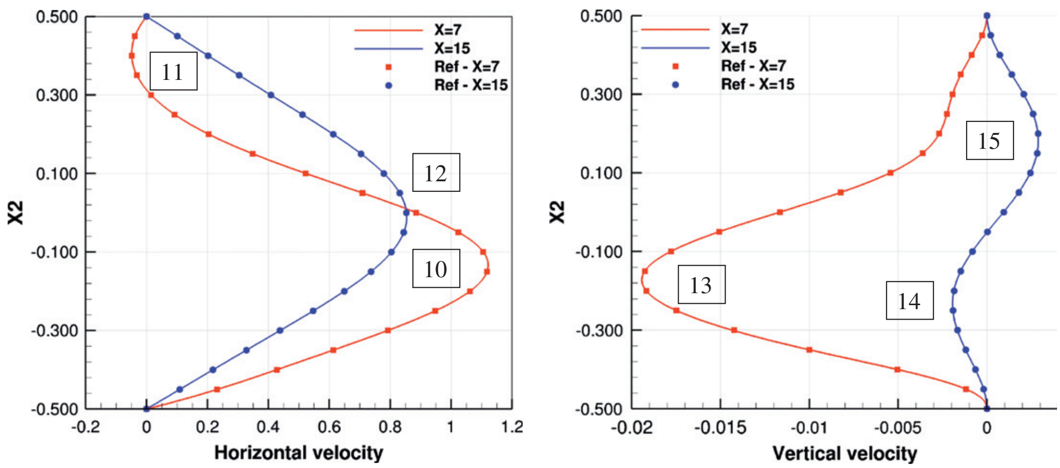

Fig. 13. Horizontal and vertical velocity across the channel at $x = 7$ and $x = 15$. Ref. from Gartling [15].

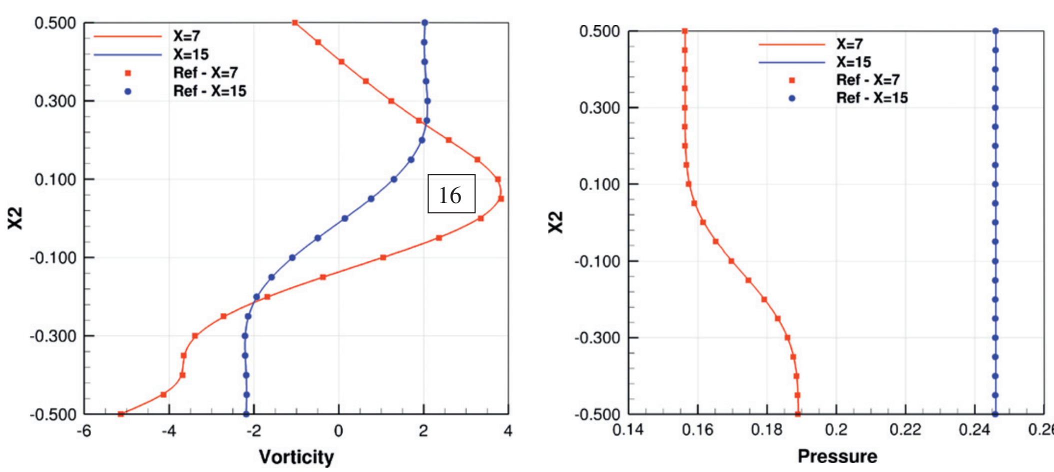

Fig. 14. Vorticity and pressure across the channel at $x = 7$ and $x = 15$. Ref. from Gartling [15].

[36]. In both studies, a first order space convergence rate is obtained, which is caused, we presume, by the singularity of the geometry at the corners of the domain [9].

We decided to push further the analysis of this case by computing the flow for various values of *Re* by varying the inlet velocity while remaining in laminar flow regime. As illustrated in Fig. 17, we observed that the eddies C, B and A appear in that order when the Reynolds number increases. We have determined the critical Reynolds number of apparitions of those three recirculations listed in the Table 7.

For the different Reynolds numbers we detailed in Table 8 the values of the extrapolated parameters with the convergence rates

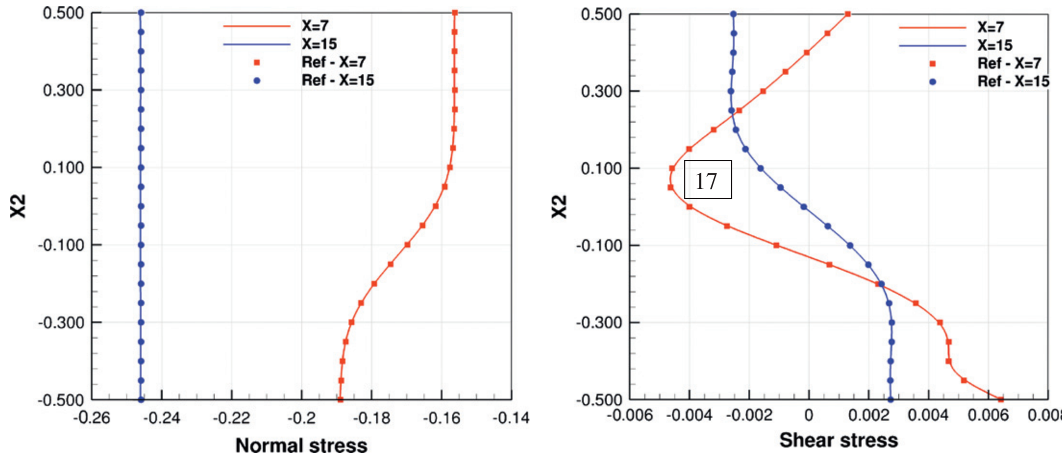

Fig. 15. Normal and shear stress across the channel at $x = 7$ and $x = 15$. Ref. from Gartling [15].

Table 3
Positions, values and convergence order of some extrema. The value and position are extracted from the finest mesh if there is no convergence order, from an extrapolated solution otherwise.

Extremum	Order	X1	X2	Values
1	2.30	$1.1085 \times 10^{+0}$	5.0000×10^{-1}	-1.5357×10^{-1}
2	–	$1.4699 \times 10^{+1}$	5.0000×10^{-1}	8.0202×10^{-2}
3	2.30	$6.3625 \times 10^{+0}$	-5.0000×10^{-1}	3.7169×10^{-2}
4	2.39	$7.7525 \times 10^{+0}$	-5.0000×10^{-1}	1.2701×10^{-2}
5	–	$1.4774 \times 10^{+1}$	-5.0000×10^{-1}	8.0158×10^{-2}
6	2.09	$8.2325 \times 10^{+0}$	5.0000×10^{-1}	1.5877×10^{-3}
7	2.26	$5.2765 \times 10^{+0}$	-5.0000×10^{-1}	-6.8583×10^{-3}
8	1.80	$7.0945 \times 10^{+0}$	-5.0000×10^{-1}	6.4549×10^{-3}
9	2.01	$1.1095 \times 10^{+1}$	-5.0000×10^{-1}	1.6905×10^{-3}
10	–	$7.0000 \times 10^{+0}$	-1.3350×10^{-1}	$1.1216 \times 10^{+0}$
11	2.09	$7.0000 \times 10^{+0}$	4.0550×10^{-1}	-4.9519×10^{-2}
12	2.06	$1.5000 \times 10^{+1}$	-1.0500×10^{-2}	8.5391×10^{-1}
13	2.12	$7.0000 \times 10^{+0}$	-1.7250×10^{-1}	-1.9083×10^{-2}
14	1.97	$1.5000 \times 10^{+1}$	-2.3350×10^{-1}	-1.9686×10^{-3}
15	2.00	$1.5000 \times 10^{+1}$	1.8150×10^{-1}	2.8398×10^{-3}
16	1.98	$7.0000 \times 10^{+0}$	6.8500×10^{-2}	$3.8128 \times 10^{+0}$
17	1.99	$7.0000 \times 10^{+0}$	7.1500×10^{-2}	-4.6368×10^{-3}

listed in Table 9. Finally, a description of the eddies (position for the finest mesh) is given in Table 10.

3.3.3. Flow past a square section cylinder

We consider the two dimensional unsteady flow past a square cylinder studied by [41,34,23,35,32] with a normal incidence and $Re = 100$. The Reynolds number is based on the free-stream velocity ($u_\infty = 1\ \mathrm{m\,s^{-1}}$), the square width $H = 1$ m, the density $\rho = 1\ \mathrm{kg\,m^{-3}}$ and the viscosity $\nu = 0.001\ \mathrm{m\,s^{-2}}$. We consider two computational domains where the distance between the outflow boundary condition and the cylinder is respectively 6H and 30H:

$$\Omega_1 = [-10.5, 6.5] \times [-10.5, 10.5]$$
$$\Omega_2 = [-10.5, 30.5] \times [-10.5, 10.5]$$

The inflow boundary at $\{x_1 = -10.5\}$ is a Dirichlet condition set to a constant horizontal flow, the outflow boundary at $\{x_1 = 6.5\}$ or $\{x_1 = 30.5\}$ is the proposed boundary condition. A symmetry condition is imposed on the upper and lower boundaries. The no-slip condition is enforced on the square obstacle placed at $(x_1, x_2) = (0, 0)$. The meshes have around two million nodes with a constant space step of 0.002 in the sub-domain

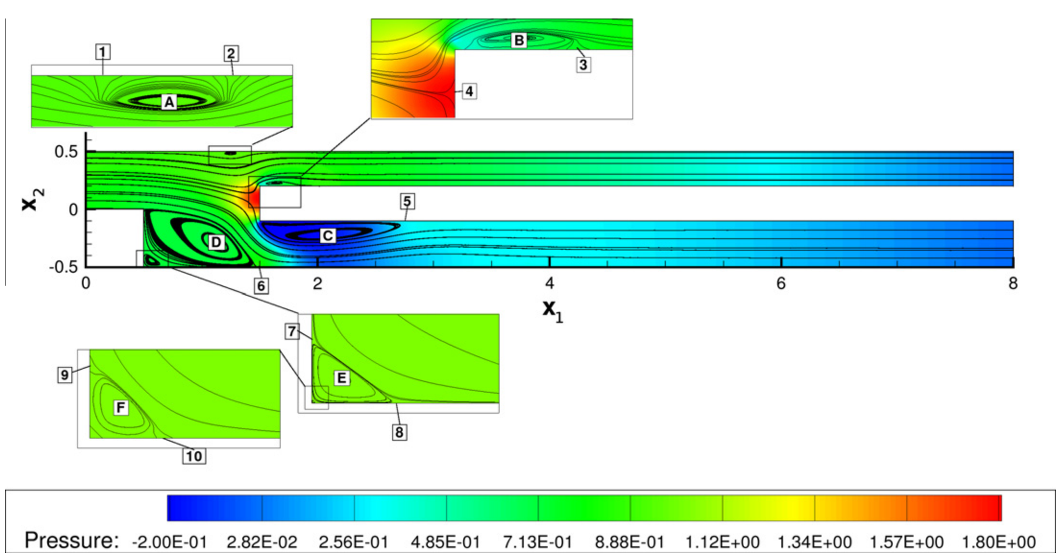

Fig. 16. Steady state of the bifurcation case at Reynolds number equal to 600. Pressure and streamlines. Eddies are numbered with letters.

Table 4
Details of some parameters in the bifurcated tube for different meshes.

	Space step size	0.02	0.01	0.005	0.0025	0.00125
Velocity correction	Total kinetic energy	$2.0144 \times 10^{+0}$	$2.0025 \times 10^{+0}$	$1.9965 \times 10^{+0}$	$1.9937 \times 10^{+0}$	$1.9922 \times 10^{+0}$
	Top outflux	1.9802×10^{-1}	1.9621×10^{-1}	1.9506×10^{-1}	1.9445×10^{-1}	1.9412×10^{-1}
	Bottom outflux	3.0118×10^{-1}	3.0359×10^{-1}	3.0489×10^{-1}	3.0554×10^{-1}	3.0587×10^{-1}
	Top charge drop	4.2242×10^{-1}	4.1188×10^{-1}	4.0563×10^{-1}	4.0234×10^{-1}	4.0058×10^{-1}
	Bottom charge drop	4.2118×10^{-1}	4.1129×10^{-1}	4.0534×10^{-1}	4.0220×10^{-1}	4.0052×10^{-1}
Pressure correction	Total kinetic energy	$2.0142 \times 10^{+0}$	$2.0025 \times 10^{+0}$	$1.9965 \times 10^{+0}$	$1.9937 \times 10^{+0}$	$1.9923 \times 10^{+0}$
	Top outflux	1.9803×10^{-1}	1.9623×10^{-1}	1.9505×10^{-1}	1.9443×10^{-1}	1.9410×10^{-1}
	Bottom outflux	3.0117×10^{-1}	3.0357×10^{-1}	3.0490×10^{-1}	3.0556×10^{-1}	3.0589×10^{-1}
	Top charge drop	4.2338×10^{-1}	4.1251×10^{-1}	4.0639×10^{-1}	4.0309×10^{-1}	4.0131×10^{-1}
	Bottom charge drop	4.2223×10^{-1}	4.1189×10^{-1}	4.0607×10^{-1}	4.0292×10^{-1}	4.0123×10^{-1}

Table 5
Extrapolation of some parameters in the bifurcated tube.

	Pressure correction		Velocity correction	
	Extrapolated value	Extrapolation order	Extrapolated value	Extrapolation order
Total kinetic energy	$1.9909 \times 10^{+0}$	1.07	$1.9909 \times 10^{+0}$	1.04
Top outflux	1.9374×10^{-1}	0.92	1.9375×10^{-1}	0.91
Bottom outflux	3.0623×10^{-1}	1.01	3.0622×10^{-1}	0.98
Top charge drop	3.9924×10^{-1}	0.89	3.9861×10^{-1}	0.92
Bottom charge drop	3.9925×10^{-1}	0.89	3.9861×10^{-1}	0.91

Table 6
Details of eddies characteristics in the bifurcated tube for different meshes.

Δx	0.02	0.01	0.005	0.0025	0.00125
Eddy A x_1	$1.2512 \times 10^{+0}$	$1.2534 \times 10^{+0}$	$1.2574 \times 10^{+0}$	$1.2594 \times 10^{+0}$	$1.2605 \times 10^{+0}$
Eddy A x_2	4.7814×10^{-1}	4.7687×10^{-1}	4.7457×10^{-1}	4.7364×10^{-1}	4.7308×10^{-1}
Eddy A ω	5.6046×10^{-1}	6.0321×10^{-1}	6.8091×10^{-1}	7.0220×10^{-1}	7.1599×10^{-1}
Point 1 x_1	$1.2000 \times 10^{+0}$	$1.1200 \times 10^{+0}$	$1.0850 \times 10^{+0}$	$1.0700 \times 10^{+0}$	$1.0600 \times 10^{+0}$
Point 2 x_1	$1.3000 \times 10^{+0}$	$1.3400 \times 10^{+0}$	$1.3600 \times 10^{+0}$	$1.3725 \times 10^{+0}$	$1.3763 \times 10^{+0}$
Eddy B x_1	$1.6449 \times 10^{+0}$	$1.6257 \times 10^{+0}$	$1.6234 \times 10^{+0}$	$1.6225 \times 10^{+0}$	$1.6219 \times 10^{+0}$
Eddy B x_2	2.2610×10^{-1}	2.2515×10^{-1}	2.2236×10^{-1}	2.2070×10^{-1}	2.1971×10^{-1}
Eddy B ω	$-8.4235 \times 10^{+0}$	$-1.0070 \times 10^{+1}$	$-9.1217 \times 10^{+0}$	$-8.5555 \times 10^{+0}$	$-8.2186 \times 10^{+0}$
Point 3 x_1	$1.7600 \times 10^{+0}$	$1.8100 \times 10^{+0}$	$1.8200 \times 10^{+0}$	$1.8175 \times 10^{+0}$	$1.8163 \times 10^{+0}$
Point 4 x_2	1.0000×10^{-1}	1.0000×10^{-1}	1.0000×10^{-1}	1.0000×10^{-1}	9.8750×10^{-2}
Eddy C x_1	$2.1183 \times 10^{+0}$	$2.0943 \times 10^{+0}$	$2.0844 \times 10^{+0}$	$2.0803 \times 10^{+0}$	$2.0784 \times 10^{+0}$
Eddy C x_2	-2.1843×10^{-1}	-2.1644×10^{-1}	-2.1498×10^{-1}	-2.1406×10^{-1}	-2.1356×10^{-1}
Eddy C ω	$1.0540 \times 10^{+1}$	$1.0179 \times 10^{+1}$	$9.9618 \times 10^{+0}$	$9.8571 \times 10^{+0}$	$9.8138 \times 10^{+0}$
Point 5 x_1	$2.7800 \times 10^{+0}$	$2.7900 \times 10^{+0}$	$2.7950 \times 10^{+0}$	$2.7975 \times 10^{+0}$	$2.7975 \times 10^{+0}$
Eddy D x_1	$1.1225 \times 10^{+0}$	$1.1340 \times 10^{+0}$	$1.1384 \times 10^{+0}$	$1.1402 \times 10^{+0}$	$1.1410 \times 10^{+0}$
Eddy D x_2	-2.9329×10^{-1}	-2.9682×10^{-1}	-2.9818×10^{-1}	-2.9873×10^{-1}	-2.9898×10^{-1}
Eddy D ω	$-2.7663 \times 10^{+0}$	$-2.7887 \times 10^{+0}$	$-2.7943 \times 10^{+0}$	$-2.7948 \times 10^{+0}$	$-2.7945 \times 10^{+0}$
Point 6 x_1	$1.4400 \times 10^{+0}$	$1.4600 \times 10^{+0}$	$1.4700 \times 10^{+0}$	$1.4725 \times 10^{+0}$	$1.4750 \times 10^{+0}$
Eddy E x_1	5.6856×10^{-1}	5.6460×10^{-1}	5.6230×10^{-1}	5.6094×10^{-1}	5.6023×10^{-1}
Eddy E x_2	-4.4270×10^{-1}	-4.4497×10^{-1}	-4.4646×10^{-1}	-4.4729×10^{-1}	-4.4772×10^{-1}
Eddy E ω	2.9552×10^{-2}	2.6009×10^{-2}	2.4410×10^{-2}	2.3541×10^{-2}	2.3089×10^{-2}
Point 7 x_2	-3.8000×10^{-1}	-3.8000×10^{-1}	-3.8000×10^{-1}	-3.8000×10^{-1}	-3.8000×10^{-1}
Point 8 x_1	6.6000×10^{-1}	6.6000×10^{-1}	6.6500×10^{-1}	6.6500×10^{-1}	6.6375×10^{-1}
Eddy F x_1	–	–	–	5.0269×10^{-1}	5.0316×10^{-1}
Eddy F x_2	–	–	–	-4.9732×10^{-1}	-4.9684×10^{-1}
Eddy F ω	–	–	–	-6.5699×10^{-5}	-1.3643×10^{-4}
Point 9 x_2	–	–	–	-4.9750×10^{-1}	-4.9375×10^{-1}
Point 10 x_1	–	–	–	5.0500×10^{-1}	5.0625×10^{-1}

$[-2, 4] \times [-2, 2]$. Step size increases toward the boundaries. The initialization of pressure is made with $p^0 = 0$. To destabilize the solution, an unsymmetrical velocity field is initialized: for $x_2 > 0$ $\boldsymbol{u}^0 = (1.1, 0)$ and, for $x_2 < 0, \boldsymbol{u}^0 = (0.9, 0)$. The computations are made with $\Delta t = 0.003$.

The various global parameters characterizing the flow are defined as:

- The lift coefficient: $C_L = \frac{2F_{x_2}}{\rho u_\infty H}$.
- The drag coefficient: $C_D = \frac{2F_{x_1}}{\rho u_\infty H}$.

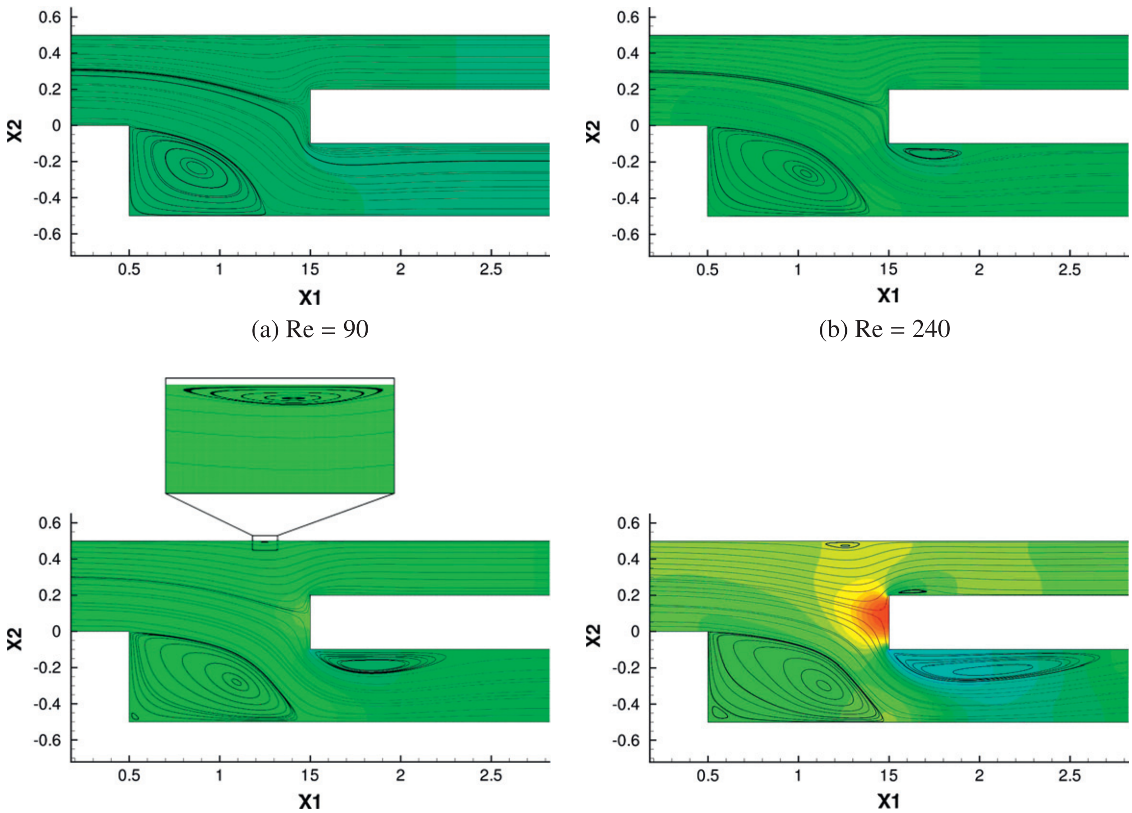

(a) Re = 90 (b) Re = 240

(c) Re = 345 (d) Re = 600

Fig. 17. Steady state of the bifurcation case for various Reynolds numbers. Pressure and streamlines.

Table 7
Critical Reynolds number of eddy appearance in the bifurcated tube for different meshes.

Space step size	0.02	0.01	0.005	0.0025	Extrapolation	Order
Eddy A	504	375	336	320	312	1.61
Eddy B	457	394	375	367	363	1.60
Eddy C	123	118	116	114	111	0.81

- The Strouhal number: $St = \frac{fH}{U_\infty}$.

where f is the shedding frequency. F_{x_1} and F_{x_2} are the sums of both pressure and viscous forces in the x_1 and x_2 directions around the Γ_c boundary of the cylinder: $(F_{x_1}, F_{x_2}) = \int_{\Gamma_c} \sigma \cdot \boldsymbol{n}$ where σ is the Cauchy stress tensor.

The result is a periodic Bénard–von Kármán vortex street shown in Fig. 18 where one can see the vorticity in the two domains at the same phase (first time step just after the sign change of the rotational at $(x_1, x_2) = (1, 0)$). As we can see, the boundary condition does not affect the flow excessively. Indeed the slight perturbations it can produce remain near itself. Values of the Strouhal number, the lift coefficient and the drag coefficient are detailed in Table 11, and are in agreement with the literature and very close with the results we detailed in [36].

Table 9
Extrapolation order of the extrapolation of some parameters in the bifurcated tube for different Reynolds numbers.

Re	90	240	345	600
Total kinetic energy	1.35	1.19	1.12	1.04
Top outflux[a]	0.19	0.75	0.83	0.91
Bottom outflux	1.27	0.99	0.97	0.98
Top charge drop	1.49	1.08	0.99	0.92
Bottom charge drop	1.66	1.10	1.00	0.91

[a] In Table 9, the convergence rate of the top outflux degrades when the Reynolds number diminishes. This is due to the coarsest mesh and is not representative of the accuracy of the computation since the convergence rate for $Re = 90$ computed with the three finest meshes is 0.79. We also computed the convergence rate of the total outflux: 2.00 and the difference of outflux between up and bottom: 1.00. This counter-intuitive behaviour has been confirmed with pressure-correction methods.

Table 8
Details of some parameters in the bifurcated tube for different Reynolds numbers. Extrapolated values.

Re	90	240	345	600
Total kinetic energy	4.2416×10^{-2}	3.0641×10^{-1}	6.5142×10^{-1}	$1.9909 \times 10^{+0}$
Top outflux	2.3749×10^{-2}	6.7754×10^{-2}	1.0263×10^{-1}	1.9375×10^{-1}
Bottom outflux	5.1231×10^{-2}	1.3223×10^{-1}	1.8734×10^{-1}	3.0622×10^{-1}
Top charge drop	5.9172×10^{-2}	1.5774×10^{-1}	2.2922×10^{-1}	3.9861×10^{-1}
Bottom charge drop	5.9168×10^{-2}	1.5774×10^{-1}	2.2922×10^{-1}	3.9861×10^{-1}

Table 10
Details of eddies characteristics in the bifurcated tube for different Reynolds numbers with the finest mesh.

Re	90	240	345	600
Eddy A x_1	–	–	$1.2495 \times 10^{+0}$	$1.2605 \times 10^{+0}$
Eddy A x_2	–	–	4.9233×10^{-1}	4.7308×10^{-1}
Eddy A ω	–	–	9.7070×10^{-2}	7.1599×10^{-1}
Point 1 x_1	–	–	$1.1750 \times 10^{+0}$	$1.0600 \times 10^{+0}$
Point 2 x_1	–	–	$1.3081 \times 10^{+0}$	$1.3763 \times 10^{+0}$
Eddy B x_1	–	–	–	$1.6219 \times 10^{+0}$
Eddy B x_2	–	–	–	2.1971×10^{-1}
Eddy B ω	–	–	–	$-8.2186 \times 10^{+0}$
Point 3 x_1	–	–	–	$1.8163 \times 10^{+0}$
Point 4 x_2	1.0875×10^{-1}	9.8750×10^{-1}	9.6875×10^{-1}	9.8750×10^{-2}
Eddy C x_1	–	$1.7242 \times 10^{+0}$	$1.8392 \times 10^{+0}$	$2.0784 \times 10^{+0}$
Eddy C x_2	–	-1.6099×10^{-1}	-1.8960×10^{-1}	-2.1356×10^{-1}
Eddy C ω	–	$2.9173 \times 10^{+0}$	$5.0853 \times 10^{+0}$	$9.8138 \times 10^{+0}$
Point 5 x_1	–	$2.0706 \times 10^{+0}$	$2.3581 \times 10^{+0}$	$2.7975 \times 10^{+0}$
Eddy D x_1	8.7315×10^{-1}	$1.0436 \times 10^{+0}$	$1.0939 \times 10^{+0}$	$1.1410 \times 10^{+0}$
Eddy D x_2	-2.3601×10^{-1}	-2.6511×10^{-1}	-2.8121×10^{-1}	-2.9898×10^{-1}
Eddy D ω	-3.5560×10^{-1}	$-1.1120 \times 10^{+0}$	$-1.6630 \times 10^{+0}$	$-2.7945 \times 10^{+0}$
Point 6 x_1	$1.2594 \times 10^{+0}$	$1.4088 \times 10^{+0}$	$1.4406 \times 10^{+0}$	$1.4750 \times 10^{+0}$
Eddy E x_1	5.1874×10^{-1}	5.2541×10^{-1}	5.3103×10^{-1}	5.6023×10^{-1}
Eddy E x_2	-4.8128×10^{-1}	-4.7481×10^{-1}	-4.6957×10^{-1}	-4.4772×10^{-1}
Eddy E ω	2.6976×10^{-3}	6.1353×10^{-3}	8.5275×10^{-3}	2.3089×10^{-2}
Point 7 x_2	-4.5625×10^{-1}	-4.4000×10^{-1}	4.2813×10^{-1}	-3.8000×10^{-1}
Point 8 x_1	5.4438×10^{-1}	5.6125×10^{-1}	5.7563×10^{-1}	6.6375×10^{-1}
Eddy F x_1	–	–	5.0143×10^{-1}	5.0316×10^{-1}
Eddy F x_2	–	–	-4.9857×10^{-1}	-4.9684×10^{-1}
Eddy F ω	–	–	-2.3526×10^{-5}	-1.3643×10^{-4}
Point 9 x_2	–	–	-4.9750×10^{-1}	-4.9375×10^{-1}
Point 10 x_1	–	–	5.0250×10^{-1}	5.0625×10^{-1}

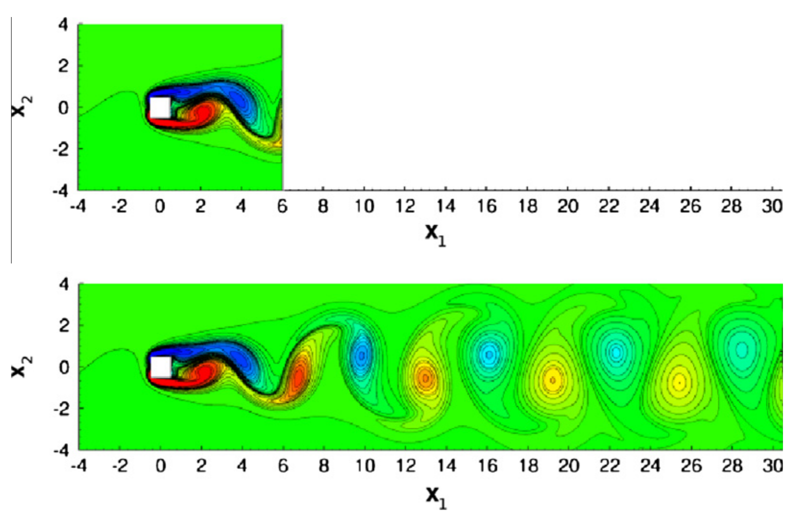

Fig. 18. Instantaneous vorticity contours for the two domains.

Table 11
Comparison of computed flow metrics.

References	St	Average C_D	r.m.s C_L
Velocity-correction 6H	0.143234	1.461273	0.152938
Velocity-correction 30H	0.147167	1.477627	0.142726
Pressure-correction [36] 6H	0.143235	1.461515	0.153056
Pressure-correction [36] 30H	0.147167	1.478745	0.142652
Sohankar et al. [41]	0.146	1.46	0.139
Pavlov et al. [34]	0.150	1.51	0.137
Hasan et al. [23]	0.144	1.40	–
Pontaza and Reddy [35]	0.140	1.48	0.141
Okajima [32] (Exp)	0.143	–	–

Acknowledgments

We acknowledge the calculation facilities financially supported by the Conseil Régional d' Aquitaine and the French Ministry of Research and Technology. This work was also granted access to the HPC resources of CINES under the allocation c2011026104 made by GENCI (Grand Equipement National de Calcul Intensif). Computer time for this study was also provided by the computing facilities MCIA (Mésocentre de Calcul Intensif Aquitain) of the Université de Bordeaux and of the Université de Pau et des Pays de l'Adour.

References

[1] Ahusborde E, Glockner S. A 2d block-structured mesh partitioner for accurate flow simulations on non-rectangular geometries. Comput Fluids 2011;43(1):2–13.

[2] Amestoy P. Multifrontal parallel distributed symmetric and unsymmetric solvers. Comput Method Appl Mech Eng April 2000;184(2–4):501–20.

[3] Arrow KJ, Hurwicz L, Uzawa H. Studies in linear and non-linear programming. Stanford: Stanford University Press; 1958.

[4] Barton IE. The entrance effect of laminar flow over a backward-facing step geometry. Int J Numer Meth Fl June 1995;25:633–44.

[5] Brown PN, Falgout RD, Jones JE. Semicoarsening multigrid on distributed memory machines. SIAM J Sci Comput 2000;21(5):1823.

[6] Bruneau CH, Fabrie P. Effective downstream boundary conditions for incompressible Navier–Stokes equations. Int J Numer Meth Fl 1994;19(8):693–705.

[7] Chorin AJ. Numerical solution of the Navier–Stokes equations. Math Comput 1968;22(104):745–62.

[8] Coutand D, Shkoller S. On the interaction between quasilinear elastodynamics and the Navier–Stokes equations. Arch Ration Mech An 2005;179(3):303–52.

[9] Dauge M. Elliptic boundary value problems in corner domains. Lect Notes Math 1988;1341:1–257.

[10] Deville MO, Fischer PF, Mund EH. High-Order methods for incompressible fluid flow. Cambridge: Cambridge University Press; 2002.

[11] Dong S, Shen J. An unconditionally stable rotational velocity-correction scheme for incompressible flows. J Comput Phys 2010;229(19):7013–29.

[12] Erturk E. Numerical solutions of 2-D steady incompressible flow over a backward-facing step, Part I: High Reynolds number solutions. Comput Fluids 2008;37(6):633–55.

[13] Févrière C, Laminie J, Poullet P, Angot P. On the penalty-projection method for the Navier–Stokes equations with the MAC mesh. J Comput Appl Math 2009;226(2):228–45.

[14] Fortin M, Glowinski R. Méthodes de Lagrangien Augmenté – Applications à la résolution numérique de problèmes aux limites. Paris: Dunod; 1982.

[15] Garling DK. A test problem for outflow boundary conditions – Flow over a backward-facing step. Int J Numer Meth Fl 1990;11:953–67.

[16] Girault V, Raviart P. Finite element methods for Navier–Stokes equations. Berlin: Springer-Verlag; 1986.

[17] Goda K. A multistep technique with implicit difference schemes for calculating two- or three-dimensional cavity flows. J Comput Phys 1979;30(1):76–95.

[18] Gresho PM, Gartling DK, Torczynski JR, Cliffe KA, Winters KH, Garratt TJ, Spence A, Goodrich JW. Is the steady viscous incompressible two-dimensional flow over a backward-facing step at $Re = 800$ stable? Int J Numer Meth Fl 1993;17:501–41.

[19] Guermond JL, Minev P, Shen J. Error analysis of pressure-correction schemes for the time-dependent Stokes equations with open boundary conditions. SIAM J Numer Anal 2005;43(1):239–58.

[20] Guermond JL, Minev P, Shen J. An overview of projection methods for incompressible flows. Comput Method Appl Mech Eng 2006;195(44–47):6011–45.

[21] Guermond JL, Shen J. Velocity-correction projection methods for incompressible flows. SIAM J Numer Anal 2004;41:112–34.

[22] Harlow FH, Welch JE. Numerical calculation of time-dependent viscous incompressible flow of fluid with free surface. Phys Fluids 1965;8(12):2182–9.

[23] Hasan N, Anwer S, Sanghi S. On the outflow boundary condition for external incompressible flows: a new approach. J Comput Phys 2005;206(2):661–83.

[24] Hypre. Hypre high performance preconditionner user's manual. Center for Applied Scientific Computing, Lawrence Livermore National Laboratory; 2008. <http://acts.nersc.gov/hypre/>

[25] Karniadakis GE, Israeli M, Orszag SA. High-order splitting methods for the incompressible Navier–Stokes equations. J Comput Phys 1991;97(2):414–43.

[26] Leriche E, Labrosse G. High-order direct Stokes solvers with or without temporal splitting: numerical investigations of their comparative properties. SIAM J Sci Comput 2000;22(4):1386–410.

[27] Liu J. Open and traction boundary conditions for the incompressible Navier–Stokes equations. J Comput Phys 2009;228(19):7250–67.

[28] Lyn DA. Computations of a laminar backward-facing step flow at $Re = 800$ with a spectral domain decomposition method. Int J Numer Meth Fl 1997;427:411–27.

[29] Nicolas X, Médale M, Glockner S, Gounand S. Benchmark solution for a three-dimennsional mixed convection flow. Part 1: Reference solution. Numer Heat Tr Part B: Fund 2011;60(5):325–45.

[30] Nicolas X, Médale M, Glockner S, Gounand S. Benchmark solution for a three-dimennsional mixed convection flow. Part 2: Analysis of Richardson extrapolation in the presence of a singularity. Numer Heat Tr Part B: Fund 2011;60(5):346–69.

[31] Moffatt HK. Viscous and resistive eddies near a sharp corner. J Fluid Mech 1964;18(01):1–18.

[32] Okajima A. Strouhal numbers of rectangular cylinders. J Fluid Mech 2006;123(-1):379–98.

[33] Orszag SA, Israeli M, Deville MO. Boundary conditions for incompressible flows. J Sci Comput 1986;1(1):75–111.

[34] Pavlov AN, Sazhin SS, Fedorenko RP. A conservative finite difference method and its application for the analysis of a transient flow around a square prism. Int J Numer Meth Heat Fluid Fl 2000;10(1):6–46.

[35] Pontaza J, Reddy J. Least-squares finite element formulations for viscous incompressible and compressible fluid flows. Comput Meth Appl Mech Eng 2006;195(19–22):2454–94.

[36] Poux A, Glockner S, Azaï M. Improvements on open and traction boundary conditions for Navier–Stokes time-splitting methods. J Comput Phys 2011;230(10):4011–27.

[37] Richardson LF, Gaunt JA. The deferred approach to the limit. Part I. Single lattice. Part II. Interpenetrating lattices. Philos Trans Roy Soc London. Series A, Cont Papers Math Phys Charact 1927;226:299–361.

[38] Roache PJ. Verification and validation in computational science and engineering. Albuquerque: Hermosa Publishers; 1998.

[39] Sani RL, Gresho PM. Résumé and remarks on the open boundary condition minisymposium. Int J Numer Meth Fl 1994;18(10):983–1008.

[40] Schaffer S. A semicoarsening multigrid method for elliptic partial differential equations with highly discontinuous and anisotropic coefficients. SIAM J Sci Comput 1998;20(1):228–42.

[41] Sohankar A, Norberg C, Davidson L. Low-Reynolds-number flow around a square cylinder at incidence: study of blockage, onset of vortex shedding and outlet boundary condition. Int J Numer Meth Fl 1998;26(1):39–56.

[42] Témam R. Navier stokes equations: theory and numerical analysis. Amsterdam: North-Holland Pub. Co.; 1984.

[43] Timmermans LJP, Minev PD, Van De Voss FN. An approximate projection scheme for incompressible flow using spectral elements. Int J Numer Meth Fl 1996;22(7):673–88.

[44] Tsynkov S. Numerical solution of problems on unbounded domains. A review. Appl Numer Math 1998;27(4):465–532.